SIAM J. Imaging Sciences
Vol. 16, No. 3, pp. 1535–1571

Imaging a Moving Point Source from Multifrequency Data Measured at One and Sparse Observation Directions (Part I): Far-Field Case*

Hongxia Guo†, Guanghui Hu†, and Guanqiu Ma‡

Abstract. We propose a multifrequency algorithm for recovering partial information on the trajectory of a moving point source from one and sparse far-field observation directions in the frequency domain. The starting and terminal time points of the moving source are both supposed to be known. We introduce the concept of observable directions (angles) in the far-field region and derive all observable directions (angles) for straight and circular motions. The existence of nonobservable directions makes this paper much different from inverse stationary source problems. At an observable direction, it is verified that the smallest strip containing the trajectory and perpendicular to the direction can be imaged, provided the angle between the observation direction and the velocity vector of the moving source lies in $[0, \pi/2]$. If otherwise, one can only expect to recover a strip thinner than this smallest strip for straight and circular motions. The far-field data measured at sparse observable directions can be used to recover the Θ-convex domain of the trajectory. Both two- and three-dimensional numerical examples are implemented to show effectiveness and feasibility of the approach.

Key words. inverse moving source problem, Helmholtz equation, multifrequency data, factorization method, uniqueness

MSC code. 35J05

DOI. 10.1137/23M1545045

1. Introduction.

1.1. Time-dependent model and Fourier transform.

We suppose that the whole space $\mathbb{R}^d$ $(d = 2, 3)$ is filled with a homogeneous and isotropic medium with a unit mass density. Consider a moving point source along the trajectory function $a(t) : [t_{\min}, t_{\max}] \to \mathbb{R}^d \in C^1[t_{\min}, t_{\max}]$ with $0 < t_{\min} < t_{\max}$. The source function S is supposed to radiate wave signals at the beginning time $t_{\min}$ and stop radiating at the time point $t_{\max}$, i.e.; it is supported in the interval $[t_{\min}, t_{\max}]$ with respect to the time variable $t > 0$. In this paper, we suppose that the source function takes the form

$$S(x, t) = g_\epsilon(x - a(t))\, \chi(t), \tag{1.1}$$

*Received by the editors January 4, 2023; accepted for publication (in revised form) April 24, 2023; published electronically August 17, 2023.
https://doi.org/10.1137/23M1545045
Funding: The work of the second author was partially supported by the National Natural Science Foundation of China (grant 12071236), the Fundamental Research Funds for Central Universities in China (grant 63213025), and a Key Program (grant 21JCZDJC00220) of Natural Science Foundation of Tianjin, China.
†School of Mathematical Sciences and LPMC, Nankai University, Tianjin, 300071, China (hxguo_math@163.com, ghhu@nankai.edu.cn).
‡Corresponding author. School of Mathematical Sciences and LPMC, Nankai University, Tianjin, 300071, China (gqma@nankai.edu.cn).

where $g_\epsilon \in C_0^\infty(\mathbb{R}^d)$ and $g_\epsilon(x) \to \delta(x)$ in the distributional sense as $\epsilon \to 0$. Here, δ denotes the Dirac delta function and

$$\chi(t) = \begin{cases} 1, & t \in [t_{\min}, t_{\max}], \\ 0, & t \notin [t_{\min}, t_{\max}], \end{cases}$$

is the characteristic function over the interval $[t_{\min}, t_{\max}]$. Denote the trajectory by $\Gamma := \{x : x = a(t),\, t \in [t_{\min}, t_{\max}]\}$. The propagation of the radiated wave fields $U(x,t)$ is governed by the initial value problem

$$\begin{cases} \dfrac{\partial^2 U}{\partial t^2} = \Delta U + S(x,t), & (x,t) \in \mathbb{R}^d \times \mathbb{R}^+, \\ U(x,0) = \partial_t U(x,0) = 0, & x \in \mathbb{R}^d. \end{cases} \tag{1.2}$$

The solution U can be written explicitly as the convolution of the fundamental solution G_d $(d = 2, 3)$ to the wave equation with the source term,

$$U(x,t) = G_d(x;t) * S(x,t) := \int_{\mathbb{R}^+} \int_{\mathbb{R}^d} G_d(x-y; t-\tau) S(y,\tau)\, dy d\tau, \tag{1.3}$$

where

$$G_d(x;t) = \begin{cases} \dfrac{H(t-|x|)}{2\pi\sqrt{t^2-|x|^2}} & \text{if} \quad d = 2, \\ \dfrac{\delta(t-|x|)}{4\pi|x|} & \text{if} \quad d = 3, \end{cases}$$

where H denotes the Heaviside function. In this paper the one-dimensional Fourier and inverse Fourier transforms are defined by

$$(\mathcal{F}g)(k) = \frac{1}{\sqrt{2\pi}} \int_{\mathbb{R}} g(t) e^{-ikt}\, dt, \quad (\mathcal{F}^{-1} v)(t) = \frac{1}{\sqrt{2\pi}} \int_{\mathbb{R}} v(k) e^{ikt}\, dk,$$

respectively. The Fourier transform of S is thus given by

$$f(x,k) := (\mathcal{F}S(x,\cdot))(k) = \frac{1}{\sqrt{2\pi}} \int_{\mathbb{R}} g_\epsilon(x - a(t)) \chi(t) e^{-ikt}\, dt = \frac{1}{\sqrt{2\pi}} \int_{t_{\min}}^{t_{\max}} g_\epsilon(x - a(t)) e^{-ikt}\, dt. \tag{1.4}$$

It is obvious the function $x \mapsto f(x,k)$ is compactly supported for every $k > 0$. From the expression (1.3), one deduces the Fourier transform of the wave fields U,

$$\begin{aligned} w(x,k) = (\mathcal{F}U)(x,k) &= \int_{\mathbb{R}^d} (\mathcal{F}G_d)(x-y;k)(\mathcal{F}S)(y,k)\, dy \\ &= \int_{\mathbb{R}^d} \Phi_d(x-y;k) f(y,k)\, dy. \end{aligned} \tag{1.5}$$

Here, $\Phi_d(x-y;k)$ is the fundamental solution to the Helmholtz equation $(\Delta + k^2)w = 0$, given by

$$\Phi_d(x-y;k) = \begin{cases} \dfrac{i}{4} H_0^{(1)}(k|x-y|), & d = 2, \\ \dfrac{e^{ik|x-y|}}{4\pi|x-y|}, & d = 3, \end{cases} \qquad x \neq y,\ x, y \in \mathbb{R}^d,$$

and $H_0^{(1)}$ is the Hankel function of the first kind of order zero. On the other hand, taking the Fourier transform on the wave equation yields the inhomogeneous Helmholtz equations

$$\Delta w(x,k) + k^2 w(x,k) = -f(x,k), \qquad x \in \mathbb{R}^d,\ k > 0. \tag{1.6}$$

From (1.5) we observe that w satisfies the Sommerfeld radiation condition

$$\lim_{r\to\infty} r^{\frac{d-1}{2}}(\partial_r w - ikw) = 0, \quad r = |x|, \tag{1.7}$$

which holds uniformly in all directions $\hat{x} = x/r \in \mathbb{S}^{d-1} := \{x \in \mathbb{R}^d : |x| = 1\}$.

1.2. Formulation in the frequency domain and literature review. Denote by $[k_{\min}, k_{\max}]$ an interval of wavenumbers/frequencies on the positive real axis. For every $k > 0$, the unique solution $w \in H^2_{loc}(\mathbb{R}^d)$ to (1.6)–(1.7) is given by (1.5), i.e.,

$$w(x,k) = \int_{\mathbb{R}^d} \Phi_d(x-y;k) f(y,k) dy, \quad x \in \mathbb{R}^d. \tag{1.8}$$

The Sommerfeld radiation condition leads to the asymptotic behavior of w at infinity:

$$w(x) = C_d \frac{e^{ik|x|}}{|x|^{\frac{d-1}{2}}} \{w^\infty(\hat{x},k) + \mathcal{O}(r^{-\frac{d+1}{2}})\} \quad \text{as} \quad |x| \to \infty,\ d = 2,3, \tag{1.9}$$

where $C_2 = e^{i\pi/4}/\sqrt{8\pi k}$, $C_3 = 1/4\pi$, and $w^\infty(\cdot,k) \in C^\infty(\mathbb{S}^{d-1})$ is known as the far-field pattern (or scattering amplitude) of w. It is well known that the function $\hat{x} \mapsto w^\infty(\hat{x},k)$ is real-analytic on $\mathbb{S}^{d-1}$, where $\hat{x} \in \mathbb{S}^{d-1}$ is usually referred to as the observation direction. By (1.8), the far-field pattern w^∞ of w can be expressed as

$$w^\infty(\hat{x},k) = \int_{\mathbb{R}^d} e^{-ik\hat{x}\cdot y} f(y,k)\, dy = \frac{1}{\sqrt{2\pi}} \int_{\mathbb{R}^d} e^{-ik\hat{x}\cdot y} \int_{t_{\min}}^{t_{\max}} g_\epsilon(y - a(t)) e^{-ikt}\, dt\, dy \tag{1.10}$$

for $\hat{x} \in \mathbb{S}^{d-1}$ and $k > 0$. In this paper, we will consider an ideal model in the limiting case that $\epsilon \to 0$, where the far-field pattern can be expressed as

$$w^\infty(\hat{x},k) = \frac{1}{\sqrt{2\pi}} \int_{\mathbb{R}^d} e^{-ik\hat{x}\cdot y} \int_{t_{\min}}^{t_{\max}} \delta(y - a(t)) e^{-ikt}\, dt\, dy = \frac{1}{\sqrt{2\pi}} \int_{t_{\min}}^{t_{\max}} e^{-ik(a(t)\cdot\hat{x} + t)}\, dt. \tag{1.11}$$

Noting that the time-dependent source S is real valued, we have $f(x,-k) = \overline{f(x,k)}$ for all $k > 0$ and thus $w^\infty(x,-k) = \overline{w^\infty(x,k)}$.

In this paper we are interested in the following inverse problem (see Figure 1):

(IP): Recovery the trajectory Γ from knowledge of the multifrequency far-field patterns

$$\{w^\infty(\hat{x}_j,k) : k \in [k_{\min}, k_{\max}],\ j = 1,2,\dots,M\},$$

where $\hat{x}_j \in \mathbb{S}^{d-1}$ are sparse observation directions and $[k_{\min}, k_{\max}]$ denotes a broad band of wavenumbers/frequencies.

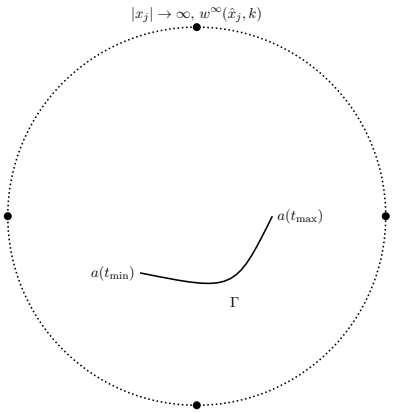

Figure 1. *Imaging the trajectory* Γ *from knowledge of multifrequency far-field patterns measured at sparse observation directions* $\hat{x}_j := (\cos(j\pi/2), \sin(j\pi/2))$, $j = 0, 1, 2, 3$.

In particular, we are interested in the following question:

What kind information on Γ can be extracted from the multifrequency far-field patterns $\{w^\infty(\hat{x}, k) : k \in [k_{\min}, k_{\max}]\}$ at a fixed observation direction $\hat{x} \in \mathbb{S}^{d-1}$?

We remark that in the stationary case that $a(t) \equiv z \in \mathbb{R}^d$, one can at most expect to recover the hyperplane $\{y \in \mathbb{R}^d : \hat{x} \cdot (y - z) = 0\}$ from the multifrequency far-field patterns $w^\infty(\hat{x}, k)$ with $k \in [k_{\min}, k_{\max}]$. The above questions are of great importance in industrial, medical, and military applications, because the number of the measurement positions is usually quite limited and multifrequency data are always available by Fourier transforming the time-dependent measurement data. Although multifrequency far-field patterns are taken as the measurement data within this paper, the approach explored here carries over naturally to the near-field data case at least in three dimensions.

To the best of the authors' knowledge, there are very few mathematical studies on direct and inverse scattering theory for moving targets, in comparison with vast literatures devoted to scattering by stationary objects (see the monograph [17]). Cooper and Strauss [4, 5] and Stefanov [27] contribute rigorous mathematical theory to direct and inverse scattering from moving obstacles. We also refer the reader to [3] for a linearized imaging theory with applications to various radar systems. Recently there has been growing research interest in detecting the motion of moving point sources governed by inhomogeneous wave equations. This kind of inverse source problem can be regarded as a linearized inverse obstacles problem. Consequently, various inversion algorithms have been proposed for recovering the orbit, profile, and magnitude of a moving point source, such as the algebraic method [24, 29, 25], the time-reversal method [8], the method of fundamental solutions [2], matched-filter and correlation-based imaging schemes [7], the iterative thresholding scheme [21], and Bayesian inference [22, 30]. See also [23, 14, 15, 16, 18] for uniqueness and stability results on inverse problems of identifying moving sources.

The purpose of this paper is to establish a factorization method for imaging the trajectory from sparse far-field measurements at multiple frequencies. The factorization method was first proposed by Kirsch in 1998 (see [19]). It has been successfully applied to various inverse

scattering problems with multistatic data at a fixed energy (or equivalently, the Dirichlet-to-Neumann map). Its multifrequency version was rigorously justified by Griesmaier and Schmiedecke [11] for inverse wavenumber-independent source problems. It was verified in [11] that the smallest strip containing the support of a stationary source and perpendicular to a single observation direction in the far field can be imaged. With sparse far-field observations, the so-called Θ-convex polygon (that is, a convex polygon whose normals coincide with observation directions) of the support can be recovered. If the dependence of the underlying source on the wavenumber takes the form of a windowed Fourier transform, one can also establish the analogue of the multifrequency factorization method [12]. The approach of [12] also provides inspirations for dealing with other kinds of wavenumber-dependent sources (or equivalently, time-dependent sources). Although preliminary tests are implemented in [12] for imaging the trajectory of a moving source, a comprehensive mathematical framework still needs to be built, which is the primary task of this work. Extensive numerical tests are implemented in the frequency domain in this paper. The counterpart of our inversion theory for wave equations using time-dependent near-field data deserves to be further investigated, which will be reported in our subsequent publications.

Motivated by earlier studies on sampling-type methods for solving inverse source problems [11, 12, 1, 13], one can at most expect to recover the smallest strip containing the trajectory and perpendicular to the observation direction through the multifrequency data measured at a single direction. The reader is also referred to [9, 10, 6, 20, 26] for imaging problems with multifrequency data or using the multistatic factorization method. However, our studies show that imaging such a strip turns out to be impossible for inverse moving source problems with a general orbit function. The recovery of the motion can be achieved only if the observation direction is *observable* in the sense of Definition 3.6 and the orbit function possesses a certain monotonicity property (that is, $h'(t) \geq 1$); see Theorem 4.4(ii) and Remark 5.1. In particular, the monotonicity can be fulfilled if the angle between the velocity vector of the moving source and an observable direction lies in $[0, \pi/2]$, and this is a sufficient and necessary condition for imaging the smallest strip if the source moves along a line segment or an arc. Otherwise, one can only get a strip $K_\Gamma^{(\hat{x})}$ (see (3.11) for the definition) whose width is not bigger than the aforementioned smallest strip at an observable direction. For nonobservable directions, the choice of the test function cannot lie in the range of the data-to-pattern operator (see Lemma 3.11). Hence, it is impossible to extract any information on the motion of a moving source by our theory, although numerics still show partial information which, however, remains unclear to us. In this paper we derive all observable and nonobservable directions (angles) for straight and circular motions. The existence of nonobservable directions makes this paper much different from inverse stationary source problems considered as in [11, 1].

Using sparse observable directions, we design an indicator function for imaging the Θ-convex domain of the trajectory. The Θ-convex domain is a subset of the Θ-convex polygon introduced in [11] and the Θ-convex scattering support in [28], because it is defined for observable directions only. Some uniqueness results will be summarized in Theorem 4.4, as a byproduct of the factorization scheme established in Theorems 4.1 and 4.2. To the best of our knowledge, the second assertion of Theorem 4.4 contributes the first uniqueness result to inverse moving source problems at a single observation direction. Finally, we highlight features of this paper as follows: (i) propose a noniterative algorithm for extracting information

on a moving point source from multifrequency data measured at one or sparse observation directions; (ii) prove a uniqueness result to inverse moving source problems using the data measured at observable directions; (iii) impose no constraint on the speed of the moving source. In our theory, the speed affects the range of nonobservable directions.

The remainder of the paper is organized as follows. In section 2, the multifrequency far-field operator $\mathcal{F}^{(\hat{x})}$ for a fixed observation $\hat{x}$ is factorized in terms of the data-to-pattern operator $\mathcal{L}^{(\hat{x})}$, following the spirit of [12]. A range identity is given to connect the ranges of $\mathcal{F}^{(\hat{x})}$ and $\mathcal{L}^{(\hat{x})}$. Section 3 is devoted to the choice of test functions for characterizing the strip $K_\Gamma^{(\hat{x})}$ through analysis on the range of the data-to-pattern operator $\mathcal{L}^{(\hat{x})}$. In section 4 we define indicator functions using the far-field data measured at one or several observable directions. Two- and three-dimensional numerical tests will be reported in the final section 5.

2. Factorization of far-field operator.

The aim of this section is to explore the factorization method for recovering the trajectory Γ from the data measured at a single observation direction $\hat{x} \in \mathbb{S}^{d-1}$. We shall proceed with the lines of [12] to derive a factorization of the far-field operator $\mathcal{F}^{(\hat{x})}$. Following the spirit of [11], we introduce the central frequency κ and half of the bandwidth of the given data K as

$$\kappa := \frac{k_{\min} + k_{\max}}{2}, \quad K := \frac{k_{\max} - k_{\min}}{2}.$$

Define the far-field operator $\mathcal{F}^{(\hat{x})} : L^2(0,K) \to L^2(0,K)$ by

$$(\mathcal{F}^{(\hat{x})}\phi)(\tau) := \int_0^K w^\infty(x, \kappa + \tau - s)\, \phi(s)\, ds, \qquad \tau \in (0,K). \tag{2.1}$$

Recall from (1.11) that w^∞ is analytic in $k \in \mathbb{R}$. Hence the far-field operator $\mathcal{F}^{(\hat{x})}$ is linear and bounded. Further, it holds that

$$\begin{aligned}(\mathcal{F}^{(\hat{x})}\phi)(\tau) &= \int_0^K \int_{\mathbb{R}^d} e^{-i(\kappa+\tau-s)\hat{x}\cdot y} f(y, \kappa+\tau-s)\, dy\, \phi(s)\, ds \\ &= \int_0^K \int_{\mathbb{R}^d} e^{-i(\kappa+\tau-s)\hat{x}\cdot y} \left(\frac{1}{\sqrt{2\pi}} \int_{t_{\min}}^{t_{\max}} e^{-i(\kappa+\tau-s)t} \delta(y - a(t))\, dt \right) dy\, \phi(s)\, ds \\ &= \frac{1}{\sqrt{2\pi}} \int_0^K \int_{t_{\min}}^{t_{\max}} e^{-i(\kappa+\tau-s)(t+\hat{x}\cdot a(t))}\, dt\, \phi(s)\, ds.\end{aligned} \tag{2.2}$$

Below we shall prove a factorization of the above far-field operator.

Theorem 2.1. *We have $\mathcal{F}^{(\hat{x})} = \mathcal{L}\mathcal{T}\mathcal{L}^*$, where $\mathcal{L} = \mathcal{L}^{(\hat{x})} : L^2(t_{\min}, t_{\max}) \to L^2(0,K)$ is defined by*

$$(\mathcal{L}\psi)(\tau) := \int_{t_{\min}}^{t_{\max}} e^{-i\tau(t+\hat{x}\cdot a(t))} \psi(t)\, dt, \quad \tau \in (0,K), \tag{2.3}$$

for all $\psi \in L^2(t_{\min}, t_{\max})$. Here the middle operator $\mathcal{T} : L^2(t_{\min}, t_{\max}) \to L^2(t_{\min}, t_{\max})$ is a multiplication operator defined by

$$(\mathcal{T}\varphi)(t) := \frac{1}{\sqrt{2\pi}} e^{-i\kappa(t+\hat{x}\cdot a(t))} \varphi(t). \tag{2.4}$$

Remark 2.2. In the remainder of this paper the operator $\mathcal{L}$ will be referred to as the data-to-pattern operator corresponding to the orbit function $a(t)$. It is obvious that the far-field data (1.11) can be expressed as $w^\infty(\hat{x},k) = (\mathcal{L}^{(\hat{x})}1)(k)$. We refer to [19] for the analogue of the data-to-pattern operator for multistatic far-field operators at a fixed frequency.

Proof. We first show that the adjoint operator $\mathcal{L}^* : L^2(0,K) \to L^2(t_{\min}, t_{\max})$ of $\mathcal{L}$ can be expressed by

$$(\mathcal{L}^*\phi)(t) := \int_0^K e^{is(t+\hat{x}\cdot a(t))}\phi(s)\,ds, \quad \phi \in L^2(0,K). \tag{2.5}$$

Indeed, for $\psi \in L^2(t_{\min}, t_{\max})$ and $\phi \in L^2(0,K)$, it holds that

$$\begin{aligned}\langle \mathcal{L}\psi, \phi\rangle_{L^2(0,K)} &= \int_0^K \left(\int_{t_{\min}}^{t_{\max}} e^{-i\tau(t+\hat{x}\cdot a(t))}\psi(t)\,dt\right)\overline{\phi(\tau)}\,d\tau \\ &= \int_{t_{\min}}^{t_{\max}} \psi(t)\left(\int_0^K \overline{e^{i\tau(t+\hat{x}\cdot a(t))}\phi(\tau)}d\tau\right)dt \\ &= \langle \psi, \mathcal{L}^*\phi\rangle_{L^2(t_{\min},t_{\max})},\end{aligned}$$

which implies (2.5). By the definition of $\mathcal{T}$, we have

$$(\mathcal{T}\mathcal{L}^*\phi)(t) = \frac{1}{\sqrt{2\pi}}e^{-i\kappa(t+\hat{x}\cdot a(t))}\int_0^K e^{is(t+\hat{x}\cdot a(t))}\phi(s)\,ds, \quad \phi \in L^2(0,K).$$

Hence, using (2.2),

$$\begin{aligned}(\mathcal{L}\mathcal{T}\mathcal{L}^*\phi)(\tau) &= \int_{t_{\min}}^{t_{\max}} e^{-i\tau(t+\hat{x}\cdot a(t))}\left(\frac{1}{\sqrt{2\pi}}e^{-i\kappa(t+\hat{x}\cdot a(t))}\int_0^K e^{is(t+\hat{x}\cdot a(t))}\phi(s)\,ds\right)dt \\ &= \frac{1}{\sqrt{2\pi}}\int_0^K \int_{t_{\min}}^{t_{\max}} e^{-i(\kappa+\tau-s)(t+\hat{x}\cdot a(t))}\,dt\,\phi(s)\,ds \\ &= (\mathcal{F}^{(\hat{x})}\phi)(\tau).\end{aligned}$$

This proves the factorization $\mathcal{F}^{(\hat{x})} = \mathcal{L}\mathcal{T}\mathcal{L}^*$. ∎

Denote by $\mathrm{Range}(\mathcal{L}^{(\hat{x})})$ the range of the data-to-pattern operator $\mathcal{L} = \mathcal{L}^{(\hat{x})}$ (see (2.3)) acting on $L^2(t_{\min}, t_{\max})$.

Lemma 2.3. *The operator $\mathcal{L} : L^2(t_{\min}, t_{\max}) \to L^2(0,K)$ is compact with dense range.*

Proof. For any $\psi \in L^2(t_{\min}, t_{\max})$, it holds that $\mathcal{L}\psi \in H^1(0,K)$, which is compactly embedded into $L^2(0,K)$. This proves the compactness of $\mathcal{L}$. By (2.5), $(\mathcal{L}^*\phi)(t)$ coincides with the inverse Fourier transform of ϕ at the variable $t + \hat{x}\cdot a(t)$. Since the set $\{t + \hat{x}\cdot a(t) : t \in [t_{\min}, t_{\max}]\}$ forms an interval of $\mathbb{R}$, the relation $(\mathcal{L}^*\phi)(t) = 0$ implies $\phi = 0$ in $L^2(0,K)$. Hence, $\mathcal{L}^*$ is injective. The denseness of $\mathrm{Range}(\mathcal{L}^{(\hat{x})})$ in $L^2(0,K)$ follows from the injectivity of $\mathcal{L}^*$. ∎

Within the framework of the factorization method, it is essential to connect the ranges of $\mathcal{F}^{(\hat{x})}$ and $\mathcal{L}$. We first recall that for a bounded operator $F : Y \to Y$ in a Hilbert space Y the real and imaginary parts of F are defined respectively by

$$\mathrm{Re}\,F = \frac{F + F^*}{2}, \quad \mathrm{Im}\,F = \frac{F - F^*}{2i},$$

which are both self-adjoint operators. Furthermore, by spectral representation we define the self-adjoint and positive operator $|\mathrm{Re}\, F|$ as

$$|\mathrm{Re}\, F| = \int_{\mathbb{R}} |\lambda|\, dE_\lambda \qquad \text{if} \quad \mathrm{Re}\, F = \int_{\mathbb{R}} \lambda\, dE_\lambda.$$

The self-adjoint and positive operator $|\mathrm{Im}\, F|$ can be defined analogously. We introduce a new operator

$$F_\# := |\mathrm{Re}\, F| + |\mathrm{Im}\, F|.$$

Since $F_\#$ is self-adjoint and positive, its square root $F_\#^{1/2}$ is defined as

$$F_\#^{1/2} := \int_{\mathbb{R}^+} \sqrt{\lambda}\, dE_\lambda \qquad \text{if} \quad F_\# = \int_{\mathbb{R}^+} \lambda\, dE_\lambda.$$

In this paper we need the following result from functional analysis.

Theorem 2.4 ([11]). *Let X and Y be Hilbert spaces, and let $F : Y \to Y$, $L : X \to Y$, $T : X \to X$ be linear bounded operators such that $F = LTL^*$. We make the following assumptions:*

(i) *L is compact with dense range, and thus L^* is compact and one-to-one.*

(ii) *$\mathrm{Re}\, T$ and $\mathrm{Im}\, T$ are both one-to-one, and the operator $T_\# = |\mathrm{Re}\, T| + |\mathrm{Im}\, T| : X \to X$ is coercive, i.e., there exists $c > 0$ with*

$$\langle T_\# \varphi, \varphi \rangle \geq c\, ||\varphi||^2 \quad \text{for all} \quad \varphi \in X.$$

Then the operator $F_\#$ is positive and the ranges of $F_\#^{1/2} : Y \to Y$ and $L : X \to Y$ coincide.

Applying Theorem 2.4 to our inverse problem, we set

$$F = \mathcal{F}^{(\hat{x})}, \quad L = \mathcal{L}, \quad T = \mathcal{T}, \quad X = L^2(t_{\min}, t_{\max}), \quad Y = L^2(0, K),$$

where $\mathcal{T}$ is the multiplication operator of (2.4). It is easy to see

$$[(\mathrm{Re}\, \mathcal{T})\, \varphi]\, (t) = \frac{1}{\sqrt{2\pi}} \cos[\kappa(t + \hat{x} \cdot a(t))] \varphi(t),$$
$$[(\mathrm{Im}\, \mathcal{T})\, \varphi]\, (t) = -\frac{1}{\sqrt{2\pi}} \sin[\kappa(t + \hat{x} \cdot a(t))] \varphi(t)$$

are both one-to-one operators from $L^2(t_{\min}, t_{\max})$ onto $L^2(t_{\min}, t_{\max})$. The coercivity assumption of $\mathcal{F}^{(\hat{x})}$ yields the coercivity of $\mathcal{T}_\#$. As a consequence of Theorem 2.4, we obtain

$$\mathrm{Range}\, [(\mathcal{F}^{(\hat{x})})_\#^{1/2}] = \mathrm{Range}\, (\mathcal{L}^{(\hat{x})}) \quad \text{for any } \hat{x} \in \mathbb{S}^{d-1}. \tag{2.6}$$

Let $\varphi \in L^2(0, K)$ be a test function. We want to characterize the range of $\mathcal{L}^{(\hat{x})}$ through the choice of φ. Denote by $(\lambda_n^{(\hat{x})}, \psi_n^{(\hat{x})})$ an eigensystem of the positive and self-adjoint operator $(\mathcal{F}^{(\hat{x})})_\#$, which is uniquely determined by the multifrequency far-field patterns $\{w^\infty(\hat{x}, k) : k \in (k_{\min}, k_{\max})\}$. Applying Picard's theorem and Theorem 2.4, we obtain

$$\varphi \in \mathrm{Range}(\mathcal{L}^{(\hat{x})}) \quad \text{if and only if} \quad \sum_{n=1}^{\infty} \frac{|\langle \varphi, \psi_n^{(\hat{x})} \rangle|^2}{|\lambda_n^{(\hat{x})}|} < +\infty. \tag{2.7}$$

To establish the factorization method, we now need to choose a proper class of test functions which usually rely on a sample variable in $\mathbb{R}^d$.

3. Range of $\mathcal{L}^{(\hat{x})}$ and test functions. To characterize the range of $\mathcal{L}^{(\hat{x})}$, we need to investigate monotonicity of the function $h(t) := \hat{x} \cdot a(t) + t \in C^1[t_{\min}, t_{\max}]$. For this purpose we define the division points of a continuous function over a closed interval.

Definition 3.1. *Let $f \in C[t_{\min}, t_{\max}]$. The point $t \in (t_{\min}, t_{\max})$ is called a division point if*
(1) $f(t) = 0$;
(2) *there exists an $\epsilon_0 > 0$ such that either $|f(t+\epsilon)| > 0$ or $|f(t-\epsilon)| > 0$ for all $0 < \epsilon < \epsilon_0$.*

Obviously, the division points constitute a subset of the zero set of a continuous function. However, a division point cannot be an interior point of the zero set. Since $a(t) \in C^1[t_{\min}, t_{\max}]$, there are finitely many division points of the function h', which we denote by $t_1 < t_2 < \cdots < t_{n-1}$. The interval $[t_{\min}, t_{\max}]$ is then divided into n subintervals $[t_{j-1}, t_j]$, $j = 1, 2, \ldots, n$, where $t_{\min} = t_0$ and $t_{\max} = t_n$. Let a_j and h_j be the restrictions of a and h to $[t_{j-1}, t_j]$, respectively. Set

$$\xi^{(\hat{x})}_{j,\min} := \inf_{t \in [t_{j-1}, t_j]} \{h_j(t)\}, \quad \xi^{(\hat{x})}_{j,\max} := \sup_{t \in [t_{j-1}, t_j]} \{h_j(t)\}, \quad j = 1, 2, \ldots n.$$

In each subinterval (t_{j-1}, t_j), one of following cases must hold:

- $h_j'(t) > 0$ for all $t \in (t_{j-1}, t_j)$. There holds
$$\xi^{(\hat{x})}_{j,\min} = t_{j-1} + \hat{x} \cdot a_j(t_{j-1}), \quad \xi^{(\hat{x})}_{j,\max} = t_j + \hat{x} \cdot a_j(t_j).$$
- $h_j'(t) < 0$ for all $t \in (t_{j-1}, t_j)$. We have
$$\xi^{(\hat{x})}_{j,\min} = t_j + \hat{x} \cdot a_j(t_j), \quad \xi^{(\hat{x})}_{j,\max} = t_{j-1} + \hat{x} \cdot a_j(t_{j-1}).$$
- $h_j'(t) = 0$ for all $t \in (t_{j-1}, t_j)$. Consequently,
$$\xi^{(\hat{x})}_{j,\min} = \xi^{(\hat{x})}_{j,\max} = t + \hat{x} \cdot a_j(t), \quad t \in [t_{j-1}, t_j].$$

Define

$$\xi^{(\hat{x})}_{\min} := \min_j \xi^{(\hat{x})}_{j,\min} = \inf_{t \in [t_{\min}, t_{\max}]} \{h(t)\}, \quad \xi^{(\hat{x})}_{\max} := \max_j \xi^{(\hat{x})}_{j,\max} = \sup_{t \in [t_{\min}, t_{\max}]} \{h(t)\}, \tag{3.1}$$

which denote the minimum and maximum of h over $[t_{\min}, t_{\max}]$, respectively. If $|h_j'(t)| > 0$, the monotonicity of the function $\xi = h_j(t)$ for $t \in [t_j, t_{j-1}]$ implies the inverse function $t = h_j^{-1}(\xi) \in C^1[\xi^{(\hat{x})}_{j,\min}, \xi^{(\hat{x})}_{j,\max}]$. Set

$$J = \{j \in \mathbb{N} : 1 \le j \le n, h_j'(t) \equiv 0, t \in (t_{j-1}, t_j)\},$$

and assume $h_j(t) \equiv c_j \in \mathbb{R}$ for $j \in J$. Note that it is possible that $J = \emptyset$.

With this notation we can rephrase the operator $\mathcal{L}^{(\hat{x})}$ defined by (2.3) as

$$
\begin{aligned}
(\mathcal{L}^{(\hat{x})}\psi)(\tau) &= \sum_{j=1}^{n} \int_{t_{j-1}}^{t_j} e^{-i\tau h_j(t)}\psi(t)\,dt \\
&= \sum_{j\notin J} \int_{t_{j-1}}^{t_j} e^{-i\tau h_j(t)}\psi(t)\,dt + \sum_{j\in J} e^{-i\tau c_j} \int_{t_{j-1}}^{t_j} \psi(t)\,dt.
\end{aligned} \tag{3.2}
$$

For $j \in J$, using $e^{-i\tau c} = \sqrt{2\pi}\mathcal{F}\delta(t-c)$ we can rewrite each term in the second sum as

$$
e^{-i\tau c_j} \int_{t_{j-1}}^{t_j} \psi(t)\,dt = \sqrt{2\pi}\mathcal{F}\delta(t-c_j) \int_{t_{j-1}}^{t_j} \psi(t)\,dt. \tag{3.3}
$$

For $j \notin J$ and $h_j'(t) > 0$, the integral in the first summation on the right-hand side of (3.2) takes the form

$$
\begin{aligned}
\int_{t_{j-1}}^{t_j} e^{-i\tau h_j(t)}\psi(t)\,dt &= \int_{\xi_{j,\min}^{(\hat{x})}}^{\xi_{j,\max}^{(\hat{x})}} e^{-i\tau\xi}\psi(h_j^{-1}(\xi))\,(h_j^{-1}(\xi))'\,d\xi \\
&= \int_{\xi_{j,\min}^{(\hat{x})}}^{\xi_{j,\max}^{(\hat{x})}} e^{-i\tau\xi}\psi(h_j^{-1}(\xi))|(h_j^{-1}(\xi))'|\,d\xi.
\end{aligned}
$$

Note that $[h_j^{-1}(\xi)]' > 0$, due to the relation $h_j'(t)[h_j^{-1}(\xi)]' = 1$. Analogously, if $h_j'(t) < 0$ for some $j \notin J$, we have $[h_j^{-1}(\xi)]' < 0$ and thus

$$
\begin{aligned}
\int_{t_{j-1}}^{t_j} e^{-i\tau h_j(t)}\psi(t)\,dt &= -\int_{\xi_{j,\min}^{(\hat{x})}}^{\xi_{j,\max}^{(\hat{x})}} e^{-i\tau\xi}\psi(h_j^{-1}(\xi))(h_j^{-1}(\xi))'\,d\xi \\
&= \int_{\xi_{j,\min}^{(\hat{x})}}^{\xi_{j,\max}^{(\hat{x})}} e^{-i\tau\xi}\psi(h_j^{-1}(\xi))|(h_j^{-1}(\xi))'|\,d\xi.
\end{aligned}
$$

Now, extending h_j^{-1} by zero from $(\xi_{j,\min}^{(\hat{x})}, \xi_{j,\max}^{(\hat{x})})$ to $\mathbb{R}$ and extending $\psi \in L^2(t_{\min}, t_{\max})$ by zero to $L^2(\mathbb{R})$, we can write each term for $j \notin J$ as

$$
\int_{t_{j-1}}^{t_j} e^{-i\tau h_j(t)}\psi(t)\,dt = \int_{\mathbb{R}} e^{-i\tau\xi}\psi(h_j^{-1}(\xi))|(h_j^{-1}(\xi))'|\,d\xi. \tag{3.4}
$$

Combining (3.2), (3.3), and (3.4), we get

$$
(\mathcal{L}^{(\hat{x})}\psi)(\tau) = \int_{\mathbb{R}} e^{-i\tau\xi} g(\xi)\,d\xi, \tag{3.5}
$$

with

$$
g(\xi) = \sum_{j\notin J} \psi(h_j^{-1}(\xi))\,|(h_j^{-1}(\xi))'| + \sum_{j\in J} \delta(\xi - c_j) \int_{t_{j-1}}^{t_j} \psi(t)\,dt.
$$

Note that g is a generalized function if $J \neq \emptyset$ and that g coincides with the inverse Fourier transform of $\mathcal{L}^{(\hat{x})}\psi$ up to some constant. Since supp $h_j^{-1} \subset [\xi_{\min}^{(\hat{x})}, \xi_{\max}^{(\hat{x})}]$ for $j \notin J$ and $c_j \in [\xi_{\min}^{(\hat{x})}, \xi_{\max}^{(\hat{x})}]$, we may estimate the support of g (equivalently, the inverse Fourier transform of $\mathcal{L}^{(\hat{x})}\psi$) as follows:

$$\operatorname{supp}(g(\xi)) \subset [\xi_{\min}^{(\hat{x})}, \xi_{\max}^{(\hat{x})}].$$

Summing up the above arguments, we arrive at

Lemma 3.2. *Let $\Gamma = \{y : y = a(t), t \in [t_{\min}, t_{\max}]\} \subset \mathbb{R}^d$ be a C^1-smooth curve with $t_{\max} > t_{\min}$. Then*

$$(\mathcal{F}^{-1}\mathcal{L}^{(\hat{x})}\psi)(\xi) = \sqrt{2\pi}\left(\sum_{j\notin J}\psi(h_j^{-1}(\xi))\,|(h_j^{-1}(\xi))'| + \sum_{j\in J}\delta(\xi - c_j)\int_{t_{j-1}}^{t_j}\psi(t)\,dt\right). \tag{3.6}$$

Moreover,

$$\operatorname{supp}(\mathcal{F}^{-1}\mathcal{L}^{(\hat{x})}\psi) \subset [\xi_{\min}^{(\hat{x})}, \xi_{\max}^{(\hat{x})}].$$

Below we provide a sufficient condition to ensure trivial intersections of the ranges of two data-to-pattern operators corresponding to different trajectories.

Lemma 3.3. *Let $\Gamma_a = \{y : y = a(t), t \in [t_{\min}, t_{\max}]\} \subset \mathbb{R}^d$ and $\Gamma_b = \{y : y = b(t), t \in [t_{\min}, t_{\max}]\} \subset \mathbb{R}^d$ be C^1-smooth curves such that*

$$\left[\inf_{t\in[t_{\min},t_{\max}]}(t+\hat{x}\cdot a(t)), \sup_{t\in[t_{\min},t_{\max}]}(t+\hat{x}\cdot a(t))\right] \bigcap \left[\inf_{t\in[t_{\min},t_{\max}]}(t+\hat{x}\cdot b(t)), \sup_{t\in[t_{\min},t_{\max}]}(t+\hat{x}\cdot b(t))\right] = \emptyset. \tag{3.7}$$

Let $\mathcal{L}_a^{(\hat{x})}$ and $\mathcal{L}_b^{(\hat{x})}$ be the data-to-pattern operators associated with Γ_a and Γ_b, respectively. Then $\operatorname{Range}(\mathcal{L}_a^{(\hat{x})}) \cap \operatorname{Range}(\mathcal{L}_b^{(\hat{x})}) = \{0\}$.

Proof. Let $f_a, f_b \in L^2(t_{\min}, t_{\max})$ be such that $(\mathcal{L}_a^{(\hat{x})} f_a)(\tau) = (\mathcal{L}_b^{(\hat{x})} f_b)(\tau) := Q(\tau, \hat{x})$. We need to prove $Q(\cdot, \hat{x}) \equiv 0$. By the definition of $\mathcal{L}$ (see (2.3)), the function

$$\tau \to Q(\tau, \hat{x}) = \int_{t_{\min}}^{t_{\max}} e^{-i\tau(t+\hat{x}\cdot a(t))} f_a(t)\,dt = \int_{t_{\min}}^{t_{\max}} e^{-i\tau(t+\hat{x}\cdot b(t))} f_b(t)\,dt$$

belongs to $L^2(0, K)$. Since $Q(\tau, \hat{x})$ is analytic in $\tau \in \mathbb{R}$, the previous relation is well defined for any $\tau \in \mathbb{R}$. By Definition 3.1, we suppose that $\{t_j\}_{j=1}^{n-1}$ and $\{\tilde{t}_j\}_{j=1}^{m-1}$ are division points of the functions $h_a(t) = t + \hat{x}\cdot a(t)$ and $h_b(t) = t + \hat{x}\cdot b(t)$, respectively. Analogously we define $h_{j,a}(t) := t + \hat{x}\cdot a_j(t)$, $h_{j,b}(t) := t + \hat{x}\cdot b_j(t)$, and $J_a := \{j \in \mathbb{N} : 1 \le j \le n, h'_{j,a}(t) \equiv 0, t \in (t_{j-1}, t_j)\}$, $J_b := \{j \in \mathbb{N} : 1 \le j \le m, h'_{j,b}(t) \equiv 0, t \in (\tilde{t}_{j-1}, \tilde{t}_j)\}$. Denote $h_{j,a}(t) \equiv c_{j,a}$ for $j \in J_a$ and $h_{j,b}(t) \equiv c_{j,b}$ for $j \in J_b$. Using the formula (3.5), the function $Q(\cdot, \hat{x})$ can be rewritten as the Fourier transforms:

$$Q(\tau, \hat{x}) = \int_{\mathbb{R}} e^{-i\tau\xi} g_a(\xi, \hat{x})\,d\xi = \int_{\mathbb{R}} e^{-i\tau\xi} g_b(\xi, \hat{x})\,d\xi, \tag{3.8}$$

with

$$g_a(\xi,\hat{x}) = \sum_{j\notin J_a} f_a(h_{j,a}^{-1}(\xi))\,|(h_{j,a}^{-1}(\xi))'| + \sum_{j\in J_a}\delta(\xi - c_{j,a})\int_{t_{j-1}}^{t_j} f_a(t)\,dt,$$

$$g_b(\xi,\hat{x}) = \sum_{j\notin J_b} f_b(h_{j,b}^{-1}(\xi))\,|(h_{j,b}^{-1}(\xi))'| + \sum_{j\in J_b}\delta(\xi - c_{j,b})\int_{\tilde{t}_{j-1}}^{\tilde{t}_j} f_b(t)\,dt.$$

This implies $g_a(\xi,\hat{x}) = g_b(\xi,\hat{x})$ for all $\xi\in R$. On the other hand, the support sets of g_a and g_b satisfy

$$\operatorname{supp} g_a(\cdot,\hat{x}) \subset \left[\inf_{t\in[t_{\min},t_{\max}]}(t+\hat{x}\cdot a(t)),\ \sup_{t\in[t_{\min},t_{\max}]}(t+\hat{x}\cdot a(t))\right],$$

$$\operatorname{supp} g_b(\cdot,\hat{x}) \subset \left[\inf_{t\in[t_{\min},t_{\max}]}(t+\hat{x}\cdot b(t)),\ \sup_{t\in[t_{\min},t_{\max}]}(t+\hat{x}\cdot b(t))\right].$$

Hence, by the condition (3.7) we obtain $g_a(\xi,\hat{x}) = g_b(\xi,\hat{x}) \equiv 0$ for all $\xi\in\mathbb{R}$. In view of (3.8), we get $Q(\cdot,\hat{x})\equiv 0$. ∎

For any $y\in\mathbb{R}^d$, define the parameter-dependent test functions $\phi_y^{(\hat{x})}\in L^2(0,K)$ by

$$\phi_y^{(\hat{x})}(k) = \frac{1}{|t_{\max}-t_{\min}|}\int_{t_{\min}}^{t_{\max}} e^{-ik(\hat{x}\cdot y+t)}dt, \quad k\in(0,K). \tag{3.9}$$

Here we stress that the test function $\phi_y^{(\hat{x})}$ depends on both the observation direction $\hat{x}\in\mathbb{S}^{d-1}$ and the space variable $y\in\mathbb{R}^d$. The supporting information of the inverse Fourier transform of the above test function is described as follows.

Lemma 3.4. *We have*

$$[\mathcal{F}^{-1}\phi_y^{(\hat{x})}](\tau) = \begin{cases}\sqrt{2\pi}/|t_{\max}-t_{\min}| & \text{if} \quad \tau\in[\hat{x}\cdot y+t_{\min},\ \hat{x}\cdot y+t_{\max}],\\ 0 & \text{otherwise.}\end{cases} \tag{3.10}$$

Proof. Letting $\tau = \hat{x}\cdot y + t$, we can rewrite the function $\phi_y^{(\hat{x})}$ as

$$\phi_y^{(\hat{x})}(k) = \int_{\mathbb{R}} e^{-ik\tau} g_y(\tau,\hat{x})\,d\tau,$$

where

$$g_y(\tau,\hat{x}) := \begin{cases}\dfrac{1}{|t_{\max}-t_{\min}|} & \text{if} \quad \tau\in[\hat{x}\cdot y+t_{\min},\hat{x}\cdot y+t_{\max}],\\ 0 & \text{otherwise.}\end{cases}$$

Therefore, $[\mathcal{F}^{-1}\phi_y^{(\hat{x})}](\tau) = \sqrt{2\pi}g_y(\tau,\hat{x})$. ∎

In the following we present a necessary condition imposed on the observation direction $\hat{x}$ and radiating period $T := t_{\max}-t_{\min}$ to ensure that the test function $\phi_y^{(\hat{x})}$ lies in the range of the data-to-pattern operator.

Lemma 3.5. *If $\phi_y^{(\hat{x})} \in \mathrm{Range}(\mathcal{L}^{(\hat{x})})$ for some $y \in \mathbb{R}^d$, we have $\xi_{\max}^{(\hat{x})} - \xi_{\min}^{(\hat{x})} \geq T$. Here $\xi_{\max}^{(\hat{x})}$ and $\xi_{\min}^{(\hat{x})}$ are defined by (3.1).*

Proof. If $\phi_y^{(\hat{x})} \in \mathrm{Range}(\mathcal{L}^{(\hat{x})})$, there exists a function $\psi \in L^2(t_{\min}, t_{\max})$ such that $\phi_y^{(\hat{x})} = \mathcal{L}^{(\hat{x})}\psi$ in $L^2(0,K)$. Since both $\phi_y^{(\hat{x})}$ and $\mathcal{L}^{(\hat{x})}\psi$ are analytic functions over $\mathbb{R}$, it holds that $\phi_y^{(\hat{x})}(k) = (\mathcal{L}^{(\hat{x})}\psi)(k)$ for all $k \in \mathbb{R}$. Then their support sets must be identical, i.e., $\mathrm{supp}(\mathcal{F}^{-1}\phi_y^{(\hat{x})}) = \mathrm{supp}(\mathcal{F}^{-1}\mathcal{L}^{(\hat{x})}\phi) \subset [\xi_{\min}^{(\hat{x})}, \xi_{\max}^{(\hat{x})}]$, where we have used Lemma 3.2. Hence, the length of $\mathrm{supp}(\mathcal{F}^{-1}\phi_y^{(\hat{x})})$, which can be seen from Lemma 3.4, must be less than or equal to that of $[\xi_{\min}^{(\hat{x})}, \xi_{\max}^{(\hat{x})}]$, i.e.,

$$\xi_{\max}^{(\hat{x})} - \xi_{\min}^{(\hat{x})} \geq t_{\max} - t_{\min} = T. \qquad \blacksquare$$

From the above lemma we conclude that $\phi_y^{(\hat{x})} \notin \mathrm{Range}(\mathcal{L}^{(\hat{x})})$, for all $y \in \mathbb{R}^d$, if $\xi_{\max}^{(\hat{x})} - \xi_{\min}^{(\hat{x})} < T$. Inspired by this fact we introduce the concept of observable directions.

Definition 3.6. *Let $\xi_{\min}^{(\hat{x})}$ and $\xi_{\max}^{(\hat{x})}$ be the maximum and minimum of the function $h(t) = \hat{x}\cdot a(t) + t \in C^1[t_{\min}, t_{\max}]$ (see (3.1)). The unit vector $\hat{x} \in \mathbb{S}^{d-1}$ is called an observable direction if $\xi_{\max}^{(\hat{x})} - \xi_{\min}^{(\hat{x})} \geq T$. The direction $\hat{x}$ is called nonobservable if $\xi_{\max}^{(\hat{x})} - \xi_{\min}^{(\hat{x})} < T$.*

Remark 3.7. If the point source remains stationary, for instance, $a(t) \equiv z \in \mathbb{R}^d$, then each direction $\hat{x} \in \mathbb{S}^{d-1}$ is observable. In other words, nonobservable directions are caused by the movement of the source term.

We remark that the set of observable directions is uniquely determined by the orbit function $a(t)$ together with the starting and terminal time points $t_{\min}$ and $t_{\max}$. For nonobservable directions $\hat{x}$, one cannot extract information on the orbit function by our approach, which will be explained in the second assertion of Theorem 4.1. If $\hat{x}$ is observable and $\hat{x} \cdot a'(t) \geq 0$, the smallest strip containing the trajectory and perpendicular to $\hat{x}$ can be recovered for straight and circular motions. For other observable directions, a thinner strip perpendicular to $\hat{x}$ can be imaged. Below we derive observable directions for straight (see Figure 2) and circular motions (see Figure 3) in two dimensions. Further discussions on piecewise linear curves in two dimensions and a straight line segment in three dimensions will be presented in section 5.

Example 1: *A straight line segment in $\mathbb{R}^2$.* Suppose that an acoustic point source is moving along the straight line $a(t) = ct(\cos\alpha, \sin\alpha) \in \mathbb{R}^2$ for $t \in [t_{\min}, t_{\max}]$, where $c > 0$ denotes the velocity and $\alpha \in [0, 2\pi]$ the angle between the trajectory and the x_1-axis.

Lemma 3.8. (i) *If $c \leq 2$, the direction $\hat{x} = (\cos\theta, \sin\theta)$ is observable if $\theta \in [\alpha - \pi/2, \alpha + \pi/2]$.*
(ii) *If $c > 2$, the direction $\hat{x} = (\cos\theta, \sin\theta)$ is observable if $\theta \in [\alpha - \pi/2, \alpha + \pi/2] \cup [\alpha + \arccos(-2/c), \alpha + 2\pi - \arccos(-2/c)]$.*

Proof. From the expression of the orbit function $a(t)$, we have

$$h(t) = t + \hat{x}\cdot a(t) = t + t\,c\,(\cos\theta\cos\alpha + \sin\theta\sin\alpha) = t(1 + c\cos(\theta - \alpha)),$$
$$h'(t) = 1 + \hat{x}\cdot a'(t) = 1 + c\cos(\theta - \alpha).$$

Hence h' is a constant depending on c, θ, and α.

Case (i): If $h'(t) > 0$, then $\cos(\theta - \alpha) > -1/c$. If $\hat{x}$ is a nonobservable direction, that is, $\xi_{\max}^{(\hat{x})} - \xi_{\min}^{(\hat{x})} < T$, then it holds that

$$(t_{\max} - t_{\min})(1 + c\cos(\theta - \alpha)) < T.$$

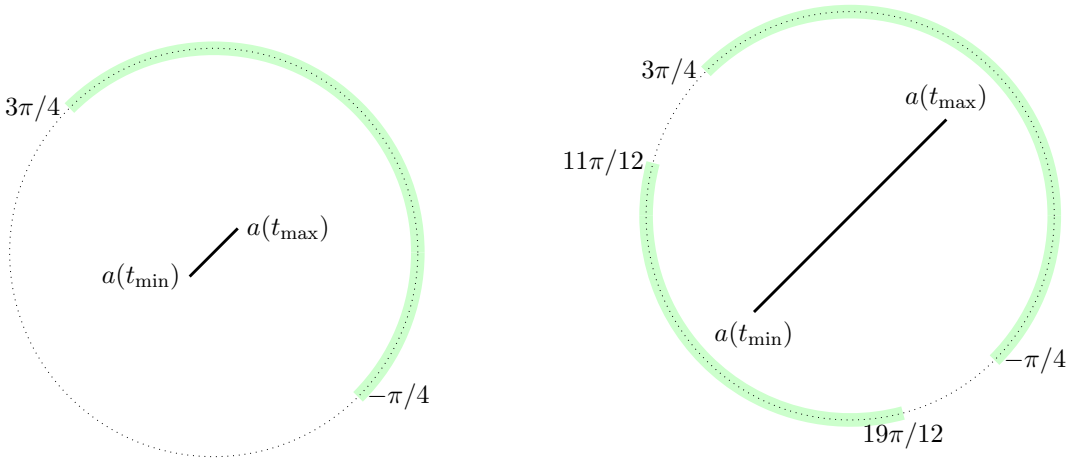

Figure 2. *Illustration of the observable (green arc) and nonobservable (dotted arc) directions for the trajectory* $a(t) = c\sqrt{2}/2(t,t)$ *for* $t \in [1,2]$ *with* $c = 1$ *(left) and* $c = 4$ *(right).*

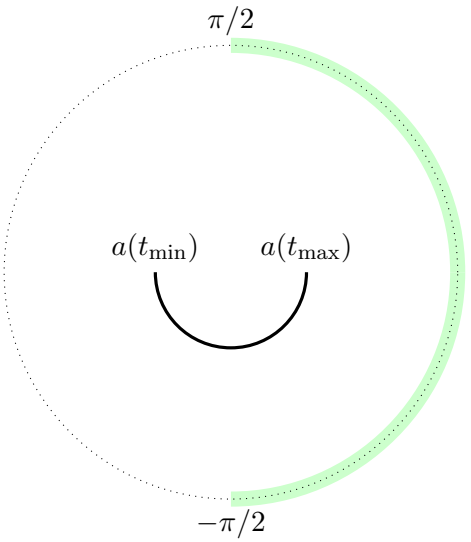

Figure 3. *Illustration of the observable (green arc) and nonobservable (dotted arc) directions for the trajectory* $a(t) = (\cos t + 1, \sin t + 2)$ *with* $t \in [\pi, 2\pi]$.

Hence, in this case $\hat{x}$ is a nonobservable direction if $-1/c < \cos(\theta - \alpha) < 0$.

Case (ii): If $h'(t) = 0$, one can deduce that each direction $\hat{x}$ is nonobservable. Note that $\cos(\theta - \alpha) = -1/c$ in such a case.

Case (iii): If $h'(t) < 0$, then $\cos(\theta - \alpha) < -1/c$. Consequently, $\hat{x}$ is a nonobservable direction only if

$$(t_{\min} - t_{\max})(1 + c\cos(\theta - \alpha)) < t_{\max} - t_{\min}.$$

Therefore, the direction $\hat{x}$ is nonobservable for $-2/c < \cos(\theta - \alpha) < -1/c$.

To sum up, we deduce that the nonobservable angles should fulfill the relation

$$-2/c < \cos(\theta - \alpha) < 0.$$

This implies that $\theta \in (\alpha + \pi/2, \alpha + 3\pi/2)$ for $c \le 2$ and $\theta \in (\alpha - \arccos(-2/c), \alpha - \pi/2) \cup (\alpha + \pi/2, \alpha + \arccos(-2/c))$ for $c > 2$. ∎

Example 2: *An arc in* $\mathbb{R}^2$. We suppose that the point source is moving along a semicircle centered at $z = (z_1, z_2) \in \mathbb{R}^2$.

Lemma 3.9. *Set* $a(t) := (\cos t + z_1, \sin t + z_2)$, $t \in [t_{\min}, t_{\max}]$, *for some* $z \in \mathbb{R}^2$. *Suppose that* $T = t_{\max} - t_{\min} < 2\pi$. *Then the direction* $\hat{x} = (\cos\theta, \sin\theta)$ *is observable if* $\theta \in [\frac{t_{\max}+t_{\min}}{2}, \frac{t_{\max}+t_{\min}}{2} + \pi]$.

Proof. We have

$$h(t) = t + \hat{x} \cdot a(t) = t + \cos(\theta - t) + \hat{x} \cdot z,$$
$$h'(t) = 1 + \hat{x} \cdot a'(t) = 1 + \sin(\theta - t).$$

It is obvious that $h'(t) > 0$ for $t \in [t_{\min}, t_{\max}]$ such that $t \neq \theta - \pi/2 + 2n\pi$, $n \in \mathbb{Z}$. Hence,

$$\xi_{\min}^{(\hat{x})} = t_{\min} + \cos(\theta - t_{\min}) + \hat{x} \cdot z, \quad \xi_{\max}^{(\hat{x})} = t_{\max} + \cos(\theta - t_{\max}) + \hat{x} \cdot z.$$

For nonobservable directions, we have

$$\cos(\theta - t_{\max}) - \cos(\theta - t_{\min}) < 0,$$

that is,

$$\sin\left(\theta - \frac{t_{\max} + t_{\min}}{2}\right) \sin\frac{t_{\max} - t_{\min}}{2} < 0.$$

Recalling from the assumption that $0 < T = t_{\max} - t_{\min} < 2\pi$, one deduces that

$$\theta \in \left(\frac{t_{\max} + t_{\min}}{2} + \pi, \frac{t_{\max} + t_{\min}}{2} + 2\pi\right).$$

Thus, $\hat{x} \in \mathbb{S}^1$ is an observable direction if $\theta \in [\frac{t_{\max}+t_{\min}}{2}, \frac{t_{\max}+t_{\min}}{2} + \pi]$. ∎

Given the trajectory $\Gamma = \{y : y = a(t), t \in [t_{\min}, t_{\max}]\}$, we define

$$\hat{x} \cdot \Gamma := \{\tau \in \mathbb{R} : \tau = \hat{x} \cdot y \text{ for some } y \in \Gamma\},$$

which is an interval of $\mathbb{R}$. Obviously, the set $\{y \in \mathbb{R}^d : \hat{x} \cdot y \in \hat{x} \cdot \Gamma\}$ denotes the smallest strip containing Γ and perpendicular to the direction $\hat{x}$. One can at most expect to recover this strip from the multifrequency data taken at a single observation direction. If $\hat{x}$ is an observable direction, we define the strip (see Figure 4)

$$K_\Gamma^{(\hat{x})} := \{y \in \mathbb{R}^d : \xi_{\min}^{(\hat{x})} - t_{\min} \le \hat{x} \cdot y \le \xi_{\max}^{(\hat{x})} - t_{\max}\} \subset \mathbb{R}^d. \tag{3.11}$$

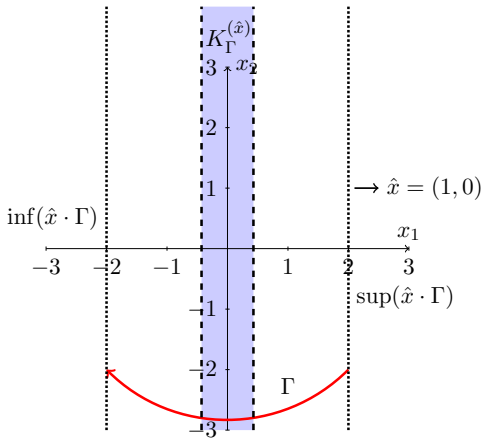

Figure 4. *Illustration of the strip* $K_\Gamma^{(\hat{x})}$ *(blue area) with* $\hat{x} = (1,0)$. *Here the curve* $a(t) = 2\sqrt{2}(\cos t, -\sin t)$, $t \in [\pi/4, 3\pi/4]$, *denotes the orbit (the red arc) of a point source moving from right to left. There holds* $\inf(\hat{x}\cdot\Gamma) = -2$, $\sup(\hat{x}\cdot\Gamma) = 2$, $\xi_{\min}^{(\hat{x})} = 3\pi/4 - 2$, $\xi_{\max}^{(\hat{x})} = \pi/4 + 2$. *In this case the strip* $K_\Gamma^{(\hat{x})}$ *is a subset of* $\{y \in \mathbb{R}^2 : \hat{x}\cdot y \in \hat{x}\cdot\Gamma\}$.

If the source remains stationary in the sense that $a(t) \equiv z$ for some $z \in \mathbb{R}^d$, the strip $K_\Gamma^{(\hat{x})}$ will be degenerated into the hyperplane $\{y \in \mathbb{R}^d : \hat{x}\cdot y = \hat{x}\cdot z\}$.

If $h'(t) > 0$ for $t \in (t_{\min}, t_{\max})$, we have

$$K_\Gamma^{(\hat{x})} = \{y \in \mathbb{R}^d : \hat{x}\cdot a(t_{\min}) \le \hat{x}\cdot y \le \hat{x}\cdot a(t_{\max})\},$$

which is a subset of $\{y \in \mathbb{R}^d : \hat{x}\cdot y \in \hat{x}\cdot\Gamma\}$. In this case, the set $K_\Gamma^{(\hat{x})}$ coincides with the strip $\{y \in \mathbb{R}^d : \hat{x}\cdot y \in \hat{x}\cdot\Gamma\}$ under the additional condition that $\hat{x}\cdot a(t_{\max}) - \hat{x}\cdot a(t_{\min}) = \sup(\hat{x}\cdot\Gamma) - \inf(\hat{x}\cdot\Gamma)$, which is in accordance with $\hat{x}\cdot a'(t) \ge 0$ for straight and circular motions.

If $h'(t) < 0$ for $t \in (t_{\min}, t_{\max})$, there holds

$$K_\Gamma^{(\hat{x})} = \{y \in \mathbb{R}^d : \hat{x}\cdot a(t_{\max}) + T \le \hat{x}\cdot y \le \hat{x}\cdot a(t_{\min}) - T\},$$

which is a subset of $\{y \in \mathbb{R}^d : \hat{x}\cdot y \in \hat{x}\cdot\Gamma\}$; see Lemma 3.10.

Lemma 3.10. *Let* $\hat{x} \in \mathbb{S}^{d-1}$ *be an observable direction. We have*

$$\hat{x}\cdot y \in \hat{x}\cdot\Gamma \quad \textit{for all} \quad y \in K_\Gamma^{(\hat{x})}.$$

Proof. Suppose that

$$\xi_{\min}^{(\hat{x})} = \hat{x}\cdot a(t_1) + t_1, \quad \xi_{\max}^{(\hat{x})} = \hat{x}\cdot a(t_2) + t_2 \quad \text{for some} \quad t_1, t_2 \in [t_{\min}, t_{\max}].$$

Therefore,

$$\xi_{\min}^{(\hat{x})} - t_{\min} = \hat{x}\cdot a(t_1) + t_1 - t_{\min} \ge \hat{x}\cdot a(t_1) \ge \inf(\hat{x}\cdot\Gamma),$$
$$\xi_{\max}^{(\hat{x})} - t_{\max} = \hat{x}\cdot a(t_2) + t_2 - t_{\max} \le \hat{x}\cdot a(t_2) \le \sup(\hat{x}\cdot\Gamma).$$

This implies that for $y \in K_\Gamma^{(\hat{x})}$,

$$\hat{x}\cdot y \geq \xi_{\min}^{(\hat{x})} - t_{\min} \geq \inf(\hat{x}\cdot\Gamma), \quad \hat{x}\cdot y \leq \xi_{\max}^{(\hat{x})} - t_{\max} \geq \sup(\hat{x}\cdot\Gamma),$$

which proves $\hat{x}\cdot y \in [\inf(\hat{x}\cdot\Gamma), \sup(\hat{x}\cdot\Gamma)] = \hat{x}\cdot\Gamma$. ∎

If $\hat{x} \in \mathbb{S}^{d-1}$ is observable, we shall prove that the test function $\phi_y^{(\hat{x})}$ lies in the range of $\mathcal{L}^{(\hat{x})}$ if and only if $y \in K_\Gamma^{(\hat{x})}$. This together with (2.6) establishes a computational criterion for imaging $K_\Gamma^{(\hat{x})}$ from the multifrequency far-field data $u^\infty(\hat{x}, k)$ with $k \in [k_{\min}, k_{\max}]$. We also need to discuss nonobservable directions.

Lemma 3.11. (i) *If $\hat{x}$ is nonobservable, we have $\phi_y^{(\hat{x})} \notin \mathrm{Range}(\mathcal{L}^{(\hat{x})})$ for all $y \in \mathbb{R}^d$.*
(ii) *If $\hat{x}$ is an observable direction, we have $\phi_y^{(\hat{x})} \in \mathrm{Range}(\mathcal{L}^{(\hat{x})})$ if and only if $y \in K_\Gamma^{(\hat{x})}$.*

Proof. (i) The first assertion follows directly from Lemma 3.5 and the Definition 3.6 for nonobservable directions.

(ii) If $\hat{x}$ is an observable direction, we have $\xi_{\max}^{(\hat{x})} - \xi_{\min}^{(\hat{x})} \geq T$. If $\phi_y^{(\hat{x})} \in \mathrm{Range}(\mathcal{L}^{(\hat{x})})$, one can find a function ϕ satisfying $\phi_y^{(\hat{x})} = \mathcal{L}^{(\hat{x})}\phi$. Then their support sets must fulfill the relation $\mathrm{supp}(\mathcal{F}^{-1}\phi_y^{(\hat{x})}) = \mathrm{supp}(\mathcal{F}^{-1}\mathcal{L}^{(\hat{x})}\phi) \subset [\xi_{\min}^{(\hat{x})}, \xi_{\max}^{(\hat{x})}]$ by Lemma 3.3. Using Lemma 3.4 yields

$$[\hat{x}\cdot y + t_{\min}, \hat{x}\cdot y + t_{\max}] \subset [\xi_{\min}^{(\hat{x})}, \xi_{\max}^{(\hat{x})}].$$

Hence, $\hat{x}\cdot y + t_{\min} \geq \xi_{\min}^{(\hat{x})}$ and $\hat{x}\cdot y + t_{\max} \leq \xi_{\max}^{(\hat{x})}$, leading to

$$\xi_{\min}^{(\hat{x})} - t_{\min} \leq \hat{x}\cdot y \leq \xi_{\max}^{(\hat{x})} - t_{\max}.$$

This proves $y \in K_\Gamma^{(\hat{x})}$.

On the other hand, if $y \in K_\Gamma^{(\hat{x})}$, we have

$$[\hat{x}\cdot y + t_{\min}, \hat{x}\cdot y + t_{\max}] \subset [\xi_{\min}^{(\hat{x})}, \xi_{\max}^{(\hat{x})}].$$

Setting

$$\psi(t) := \frac{e^{ik\hat{x}\cdot(a(t)-y)}}{|t_{\max} - t_{\min}|} \in L^2(t_{\min}, t_{\max}),$$

we find $\phi_y^{(\hat{x})}(k) = (\mathcal{L}^{(\hat{x})}\psi)(k)$. Therefore, $\phi_y^{(\hat{x})}(k) \in$ Range$(\mathcal{L}^{(\hat{x})})$. ∎

4. Indicator functions and uniqueness. If $\hat{x}$ is an observable direction, we know from Lemma 3.11 that the test functions $\phi_y^{(\hat{x})}$ can be utilized to characterize $K_\Gamma^{(\hat{x})}$ through (2.6). Hence, we define the indicator function

$$W^{(\hat{x})}(y) := \left[\sum_{n=1}^{\infty} \frac{|\langle \phi_y^{(\hat{x})}, \psi_n^{(\hat{x})}\rangle|^2_{L^2(0,K)}}{|\lambda_n^{(\hat{x})}|}\right]^{-1}, \qquad y \in \mathbb{R}^d. \tag{4.1}$$

Combining Theorem 2.4, Lemma 3.11, and Picard's theorem, we obtain the following.

Theorem 4.1 (single observable direction). *If $\hat{x}$ is an observable direction, it holds that*

$$W^{(\hat{x})}(y) = \begin{cases} 0 & \text{if} \quad y \notin K_\Gamma^{(\hat{x})}, \\ \text{finite positive number} & \text{if} \quad y \in K_\Gamma^{(\hat{x})}. \end{cases}$$

If $\hat{x}$ is nonobservable, we have $W^{(\hat{x})}(y) = 0$ for all $y \in \mathbb{R}^d$.

Hence, for observable directions the values of $W^{(\hat{x})}$ in the strip $K_\Gamma^{(\hat{x})}$ should be relatively bigger than those elsewhere. The values of $W^{(\hat{x})}$ vanish identically in $\mathbb{R}^d$ if $\hat{x}$ is nonobservable. In the case of sparse observable directions $\{\hat{x}_j : j = 1, 2, \ldots, M\}$, we shall make use of the following indicator function:

$$W(y) = \left[\sum_{j=1}^{M} \frac{1}{W^{(\hat{x}_j)}(y)} \right]^{-1} = \left[\sum_{j=1}^{M} \sum_{n=1}^{\infty} \frac{|\langle \phi_y^{(\hat{x}_j)}, \psi_n^{(\hat{x}_j)} \rangle|^2_{L^2(0,K)}}{|\lambda_n^{(\hat{x}_j)}|} \right]^{-1}, \qquad y \in \mathbb{R}^d. \tag{4.2}$$

Define the Θ-convex domain of Γ associated with the observable directions $\{\hat{x}_j : j = 1, 2, \ldots, M\}$ as

$$\Theta_\Gamma := \bigcap_{j=1,2,\ldots,M} K_\Gamma^{(\hat{x}_j)}. \tag{4.3}$$

We can reconstruct Θ_Γ from the multifrequency far-field data measured at sparse observable directions.

Theorem 4.2 (finite observable directions). *It holds that $0 < W(y) < +\infty$ if $y \in \Theta_\Gamma$, and $W(y) = 0$ if $y \notin \Theta_\Gamma$.*

Proof. If $y \in \Theta_\Gamma$, it means that $y \in K_\Gamma^{(\hat{x}_j)}$ for $j = 1, 2, \ldots, M$. By Theorem 4.1,

$$\sum_{n=1}^{\infty} \frac{|\langle \phi_y^{(\hat{x}_j)}, \psi_n^{(\hat{x}_j)} \rangle|^2_{L^2(0,K)}}{|\lambda_n^{(\hat{x}_j)}|} < +\infty \quad \text{for all} \quad j = 1, 2, \ldots, M. \tag{4.4}$$

Then the finite sum over the index j must fulfill the relation $0 < W(y) < +\infty$.

If $y \notin \Theta_\Gamma$, we may suppose without loss of generality that $y \notin K_\Gamma^{(\hat{x}_1)}$. By Theorem 4.1,

$$[W^{(\hat{x}_1)}(y)]^{-1} = \sum_{j=1}^{M} \sum_{n=1}^{\infty} \frac{|\langle \phi_y^{(\hat{x}_1)}, \psi_n^{(\hat{x}_j)} \rangle|^2_{L^2(0,K)}}{|\lambda_n^{(\hat{x}_1)}|} = \infty.$$

Together with the definition of W, this gives

$$W(y) < \left[\sum_{n=1}^{\infty} \frac{|\langle \phi_y^{(\hat{x}_1)}, \psi_n^{(\hat{x}_j)} \rangle|^2_{L^2(0,K)}}{|\lambda_n^{(\hat{x}_1)}|} \right]^{-1} = 0.$$

■

Remark 4.3. At a single observable direction, the strip $K_\Gamma^{(\hat{x})}$ coincides with $\{y \in \mathbb{R}^d : \hat{x} \cdot y \in \hat{x} \cdot \Gamma\}$ if $\hat{x} \cdot a(t_{\max}) - \hat{x} \cdot a(t_{\min}) = \sup(\hat{x} \cdot \Gamma) - \inf(\hat{x} \cdot \Gamma)$. Hence, one can obtain a convex domain

containing the trajectory Γ if the condition $\hat{x}_j \cdot a(t_{\max}) - \hat{x}_j \cdot a(t_{\min}) = \sup(\hat{x}_j \cdot \Gamma) - \inf(\hat{x}_j \cdot \Gamma)$ applies to each observable direction $\hat{x}_j$. For straight and circular motions, this condition is equivalent to $\hat{x} \cdot a'(t) \geq 0$ for all $t \in [t_{\min}, t_{\max}]$. Physically, the condition $\hat{x} \cdot a'(t) \geq 0$ means that the angle between the observable direction $\hat{x}$ and the velocity vector of the moving point source lies in $[0, \pi/2]$.

Consequently, we arrive at the following uniqueness results, which seem unknown in the literature.

Theorem 4.4 (uniqueness). *Denote by $\Gamma = \{a(t) : t \in [t_{\min}, t_{\max}]\}$ the trajectory of a moving point source where $a \in C^1[t_{\min}, t_{\max}]$.*

(i) *The Θ-convex domain of Γ associated with all observable directions $\hat{x} \in \mathbb{S}^{d-1}$ (see (4.3)) can be uniquely determined by the multifrequency data $\{u^\infty(\hat{x}, k) : \hat{x} \in \mathbb{S}^{d-1}, k \in (k_{\min}, k_{\max})\}$.*

(ii) *Let $\hat{x} \in \mathbb{S}^{d-1}$ be an arbitrarily fixed observable direction. Then the strip $K_\Gamma^{(\hat{x})}$ (see (3.11)) can be uniquely determined by the multifrequency data $\{u^\infty(\hat{x}, k) : k \in (k_{\min}, k_{\max})\}$. In particular, the strip $\{y \in \mathbb{R}^d : \hat{x} \cdot y \in \hat{x} \cdot \Gamma\}$ can be uniquely recovered if $\hat{x} \cdot a(t_{\max}) - \hat{x} \cdot a(t_{\min}) = \sup(\hat{x} \cdot \Gamma) - \inf(\hat{x} \cdot \Gamma)$ in $[t_{\min}, t_{\max}]$.*

Proof. Part (i) follows from the definition of Θ_Γ and Theorem 4.2. The second assertion (ii) is the consequence of Theorem 4.1 and Remark 4.3 in combination with the definition of $K_\Gamma^{(\hat{x})}$. ∎

The second assertion of Theorem 4.4 answers the question of what kind of information can be extracted from the multifrequency data measured at a single observable direction. Unfortunately, we do not know whether an observation direction is observable or not if there is no a priori information on the orbit function.

5. Numerical experiments in $\mathbb{R}^d$ ($d = 2, 3$). In this section, we carry out a couple of numerical experiments to validate our algorithm in both two and three dimensions. In practice, the time-domain data should be Fourier transformed to the multifrequency data, and the near-field version of our algorithm should be implemented. To simplify the numerical procedures for simulating, we shall carry out computational tests in the frequency domain only. Our aim is to get information of the trajectory of a moving point source from multifrequency far-field data taken at a single or multiple observation directions.

Suppose that the wavenumber-dependent source term $f(x, k)$ is given by (1.4). Then the far-field pattern can be synthesized by (1.11), i.e.,

$$w^\infty(\hat{x}, k) = \frac{1}{\sqrt{2\pi}} \int_{t_{\min}}^{t_{\max}} e^{-ik(\hat{x} \cdot a(t) + t)}\, dt, \quad \hat{x} \in \mathbb{R}^d\, (d = 2, 3),\ k \in (k_{\min}, k_{\max}). \tag{5.1}$$

In all our numerical examples below, we set $k_{\min} = 0$ for simplicity. The bandwidth can be extended from $(0, k_{\max})$ to $(-k_{\max}, k_{\max})$ by $w^\infty(\hat{x}, -k) = \overline{w^\infty(\hat{x}, k)}$. Then, one deduces from these new measurement data with $k_{\min} = -k_{\max}$ that $\kappa = 0$ and $K = k_{\max}$. Thus, the far field operator (2.1) becomes

$$(\mathcal{F}^{(\hat{x})}\phi)(\tau) = \int_0^{k_{\max}} w^\infty(\hat{x}, \tau - s)\, \phi(s)\, ds, \quad \tau \in (0, k_{\max}). \tag{5.2}$$

Discretize the frequency interval $(0, k_{\max})$ with

$$k_n = (n - 0.5)\Delta k, \quad \Delta k := \frac{k_{\max}}{N}, \quad n = 1, 2, \ldots, N.$$

We adopt $2N-1$ samples $w^\infty(\hat{x}, k_n)$, $n = 1, 2, \ldots, N$, and $w^\infty(\hat{x}, -k_n)$, $n = 1, 2, \ldots, N-1$, of the far field data and apply the midpoint rule to approximate the integral in (5.2). Then it follows that

$$(\mathcal{F}^{(\hat{x})}\phi)(\tau_n) \approx \sum_{m=1}^{N} w^\infty(\hat{x}, \tau_n - s_m)\phi(s_m)\Delta k, \tag{5.3}$$

where $\tau_n := n\Delta k$ and $s_m := (m - 0.5)\Delta k$, $n, m = 1, 2, \ldots, N$. Consequently, a discrete approximation of the far-field operator $\mathcal{F}^{(\hat{x})}$ is given by the Toeplitz matrix

$$F^{(\hat{x})} := \begin{pmatrix} w^\infty(\hat{x}, k_1) & \overline{w^\infty(\hat{x}, k_1)} & \cdots & \overline{w^\infty(\hat{x}, k_{N-2})} & \overline{w^\infty(\hat{x}, k_{N-1})} \\ w^\infty(\hat{x}, k_2) & w^\infty(\hat{x}, k_1) & \cdots & \overline{w^\infty(\hat{x}, k_{N-3})} & \overline{w^\infty(\hat{x}, k_{N-2})} \\ \vdots & \vdots & & \vdots & \vdots \\ w^\infty(\hat{x}, k_{N-1}) & w^\infty(\hat{x}, k_{N-2}) & \cdots & w^\infty(\hat{x}, k_1) & \overline{w^\infty(\hat{x}, k_1)} \\ w^\infty(\hat{x}, k_N) & w^\infty(\hat{x}, k_{N-1}) & \cdots & w^\infty(\hat{x}, k_2) & w^\infty(\hat{x}, k_1) \end{pmatrix} \Delta k, \tag{5.4}$$

where $\overline{w^\infty(\hat{x}, k_n)} = w^\infty(\hat{x}, -k_n)$, $n = 1, \ldots, N-1$, and $F^{(\hat{x})}$ is an $N \times N$ complex matrix.

Similarly, we discretize the test function $\phi_y^{(\hat{x})}$ from (3.9) by the vector

$$\phi_y^{(\hat{x})} := \left(\frac{i}{T\tau_1}(e^{-i\tau_1 t_{\max}} - e^{-i\tau_1 t_{\min}})\, e^{-i\tau_1 \hat{x}\cdot y}, \ \ldots, \ \frac{i}{T\tau_N}(e^{-i\tau_N t_{\max}} - e^{-i\tau_N t_{\min}})\, e^{-i\tau_N \hat{x}\cdot y} \right), \tag{5.5}$$

where $T = t_{\max} - t_{\min}$ and $\phi_y^{(\hat{x})}$ is an N-dimensional complex vector. Denoting by $\{(\tilde{\lambda}_n^{(\hat{x})}, \psi_n^{(\hat{x})}) : n = 1, 2, \ldots, N\}$ an eigensystem of the matrix $F^{(\hat{x})}$ (5.4), then one deduces that an eigensystem of the matrix $(F^{(\hat{x})})_\# := |\mathrm{Re}\,(F^{(\hat{x})})| + |\mathrm{Im}\,(F^{(\hat{x})})|$ is $\{(\lambda_n^{(\hat{x})}, \psi_n^{(\hat{x})}) : n = 1, 2, \ldots, N\}$, where $\lambda_n^{(\hat{x})} := |\mathrm{Re}\,(\tilde{\lambda}_n^{(\hat{x})})| + |\mathrm{Im}\,(\tilde{\lambda}_n^{(\hat{x})})|$. We approximate the indicator function $W^{(\hat{x})}$ of (4.1) by

$$W^{(\hat{x})}(y) := \left[\sum_{n=1}^{N} \frac{\left| \phi_y^{(\hat{x})} \cdot \overline{\psi_n^{(\hat{x})}} \right|^2}{|\lambda_n^{(\hat{x})}|} \right]^{-1}, \quad y \in \mathbb{R}^d, \tag{5.6}$$

where $\cdot$ denotes the inner product in $\mathbb{R}^d$. Accordingly, a plot of $W^{(\hat{x})}(y)$ should yield a visualization of the strip $K_\Gamma^{(\hat{x})}$, which contains information on the source trajectory if $\hat{x} \in \mathbb{S}^{d-1}$ is an observable direction. In the following numerical examples, the frequency band is taken as $(0, 3\pi)$ with $k_{\max} = 3\pi$, $N = 18$, and $\Delta k = \pi/6$.

In the following figures, the exact trajectory of a moving source is plotted with yellow solid lines. In two dimensions we shall image the trajectory of moving point sources represented by a straight line, an arc, or a piecewise linear curve, using the far-field data of one and sparse observation directions. In three dimensions, the recovery of a straight line segment is examined with the data measured at a single direction only.

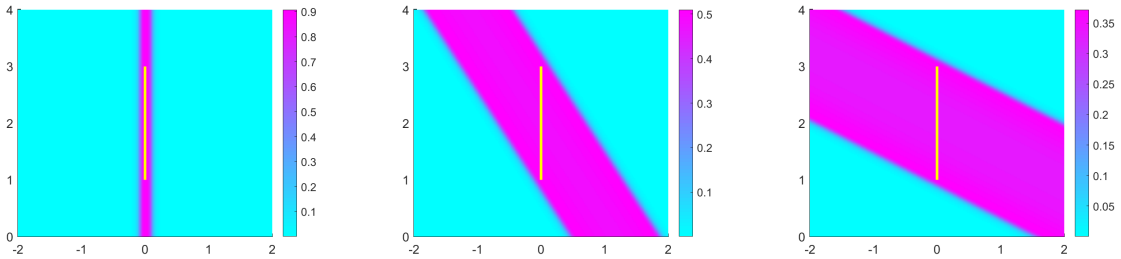

(a) $\theta = 0$ (b) $\theta = \pi/6$ (c) $\theta = \pi/3$

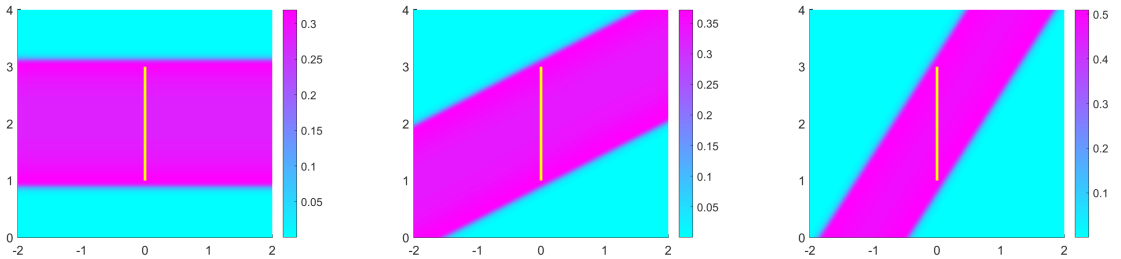

(d) $\theta = \pi/2$ (e) $\theta = 2\pi/3$ (f) $\theta = 5\pi/6$

Figure 5. *Reconstruction from a single observable direction* $\hat{x} = (\cos\theta, \sin\theta)$ *with* $\theta \in [0, \pi]$ *for a straight line segment* $a(t) = (0, t)$ *with* $t \in [1, 3]$.

5.1. A single observation direction.

Example 1: *A straight line segment in* $\mathbb{R}^2$. We consider the same straight line segment from Example 1 in section 3. The following two cases are studied.

Case 1. $c = 1$, $\alpha = \pi/2$, and $t \in [1, 3]$.

In this case the trajectory of the moving source is $a(t) = (0, t)$ for $t \in [1, 3]$. Choose the search domain as a square of the form $[-2, 2] \times [0, 4]$. By Lemma 3.8, the nonobservable directions are $\hat{x} = (\cos\theta, \sin\theta)$ with $\theta \in (\pi, 2\pi)$ and the observable directions $\hat{x} = (\cos\theta, \sin\theta)$ with $\theta \in [0, \pi]$. Numerical results are presented in Figures 5 and 6.

The observable angles are taken as $\theta = 0$, $\pi/6$, $\pi/3$, $\pi/2$, $2\pi/3$, and $5\pi/6$ in Figure 5. By Lemma 3.8, we know $K_\Gamma^{(\hat{x})} = \{y \in \mathbb{R}^2 : \inf(\hat{x} \cdot \Gamma) \le \hat{x} \cdot y \le \sup(\hat{x} \cdot \Gamma)\}$ for all observable directions, because $h'(t) = 1 + \cos(\theta - \pi/2) \ge 1$ with $t \in [1, 3]$. In Figure 5, the trajectory of the moving source is nicely located in the smallest strip $K_\Gamma^{(\hat{x})}$ perpendicular to the observation direction just as our theoretical results predict. The numerical results match well with our theoretical analysis.

Observation directions at the angles $\theta = 9\pi/8$, $10\pi/8$, $11\pi/8$, $13\pi/8$, $14\pi/8$, and $15\pi/8$ are nonobservable. The numerical results in Figure 6 show that the indicator values are all much smaller than 10^{-4}, which is quite consistent with the results of Theorem 4.1. Hence, we cannot reconstruct the smallest strip containing the trajectory of the moving source. It is very interesting to conclude from Figure 6 that, even at a nonobservable direction, partial information on the trajectory can still be recovered by our indicator function: the maximum points of $W^{(\hat{x})}$ are degenerated into a straight line perpendicular to $\hat{x}$ and passing through the middle point of the trajectory. However, this phenomenon needs to be further investigated.

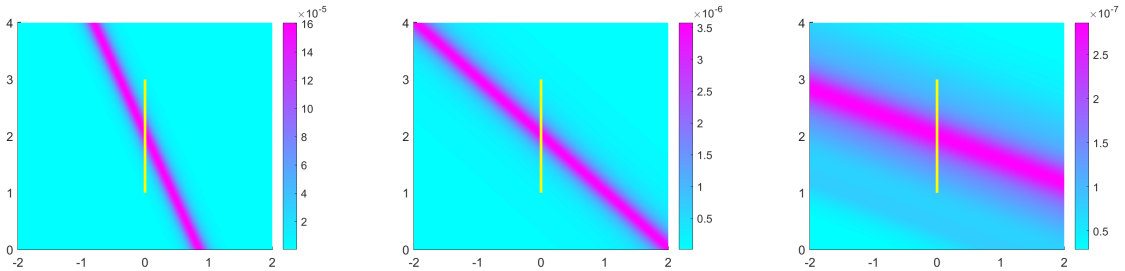

(a) $\theta = 9\pi/8$ (b) $\theta = 10\pi/8$ (c) $\theta = 11\pi/8$

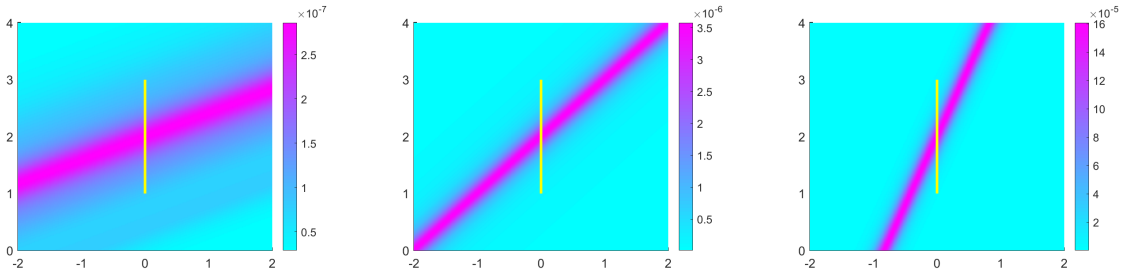

(d) $\theta = 13\pi/8$ (e) $\theta = 14\pi/8$ (f) $\theta = 15\pi/8$

Figure 6. *Reconstruction from a single nonobservable direction* $\hat{x} = (\cos\theta, \sin\theta)$ *with* $\theta \in (\pi, 2\pi)$ *for a straight line segment* $a(t) = (0, t)$ *with* $t \in [1, 3]$.

Case 2. $c = 4$, $\alpha = \pi/4$, and $t \in [1, 2]$.

In this case $a(t) = (2\sqrt{2}t, 2\sqrt{2}t)$ represents a diagonal line segment. The search domain is taken as $[-2, 5] \times [-2, 5]$. The observable directions are $\hat{x}$ with $\theta \in [0, 3\pi/4] \cup [7\pi/4, 8\pi/4] \cup [11\pi/12, 19\pi/12]$, and nonobservable directions are $\hat{x}$ with $\theta \in (3\pi/4, 11\pi/12) \cup (19\pi/12, 7\pi/4)$. By the proof of Lemma 3.8, $h'(t) = 1 + 4\cos(\theta - \pi/4) \geq 1$ for observable angles $\theta \in [0, 3\pi/4] \cup [7\pi/4, 2\pi)$, and $h'(t) < 0$ for $\theta \in [11\pi/12, 19\pi/12]$.

In Figure 7, we take different observable angles $\theta \in [0, 3\pi/4] \cup [7\pi/4, 2\pi)$. Since $h'(t) \geq 1$, the trajectory of the moving source can be completely covered by the smallest strip perpendicular to the observation direction. The numerical examples indeed show that $K_\Gamma^{(\hat{x})} = \{y \in \mathbb{R}^2 : \inf(\hat{x} \cdot \Gamma) \leq \hat{x} \cdot y \leq \sup(\hat{x} \cdot \Gamma)\}$.

In Figure 8, we measure the data at the observable angle $\theta \in [11\pi/12, 19\pi/12]$ so that $h'(t) < 0$. Although these observation directions θ belong to the class of the observable set, the recovered strips $K_\Gamma^{(\hat{x})}$ are thinner than the smallest strips containing the trajectory of the moving source, because $K_\Gamma^{(\hat{x})} \subset \{y \in \mathbb{R}^2 : \inf(\hat{x} \cdot \Gamma) \leq \hat{x} \cdot y \leq \sup(\hat{x} \cdot \Gamma)\}$ by Lemma 3.10.

In Figure 9, we make use of nonobservable angles. The numerical results illustrate that the indicator values are indeed much smaller. Hence, one cannot expect to reconstruct the smallest strip containing the trajectory of the moving source.

Example 2: *An arc in* $\mathbb{R}^2$. As shown in Example 2 of section 3, we take $a(t) = (\cos(t), \sin(t))$ with $t \in [0, \pi]$. The search domain is $[-2, 2]^2$. From Lemma 3.9, we know that observable directions are $\hat{x}$ with $\theta \in [\pi/2, 3\pi/2]$, and nonobservable directions are $\hat{x}$ with $\theta \in (0, \pi/2) \cup (3\pi/2, 2\pi)$. Figure 10 shows the reconstructions using the data from observable directions, where the subfigure (c) nicely gives us the smallest strip $K_\Gamma^{(\hat{x})}$ containing the trajectory of

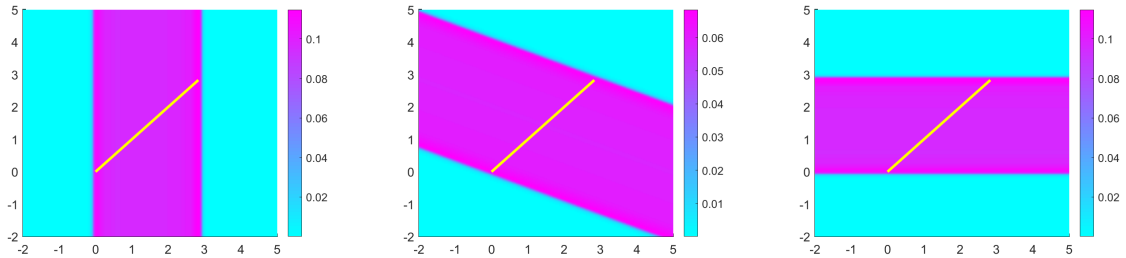

(a) $\theta = 0\pi/8$ (b) $\theta = 3\pi/8$ (c) $\theta = 4\pi/8$

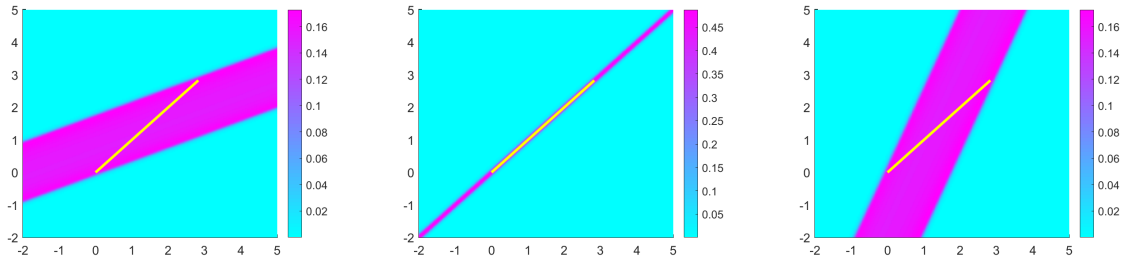

(d) $\theta = 5\pi/8$ (e) $\theta = 6\pi/8$ (f) $\theta = 15\pi/8$

Figure 7. *Reconstruction from a single observable direction* $\hat{x} = (\cos\theta, \sin\theta)$ *with* $\theta \in [0, 3\pi/4] \cup [7\pi/4, 2\pi)$ *for a straight line segment* $a(t) = (2\sqrt{2}t, 2\sqrt{2}t)$ *with* $t \in [1, 2]$. *Since* $h'(t) \geq 1$, *the strip* $K_\Gamma^{(\hat{x})}$ *coincides with* $\{y \in \mathbb{R}^2 : \hat{x} \cdot y \in \hat{x} \cdot \Gamma\}$.

the moving source that is perpendicular to the observable direction. Note that $K_\Gamma^{(\hat{x})} = \{y \in \mathbb{R}^2 : \sup(\hat{x} \cdot \Gamma) \leq \hat{x} \cdot y \leq \inf(\hat{x} \cdot \Gamma)\}$ for $8\pi/8$, because $h'(t) \geq 1$ for all $t \in [0, \pi]$. However, the strips $K_\Gamma^{(\hat{x})}$ in subfigures (a), (b), and (d) do not provide sufficient information on the trajectory. This is due to the fact that $h'(t) \geq 1$ for all $t \in [0, \pi]$ doesn't hold at $\theta = 5\pi/8$, $6\pi/8$, $10\pi/8$, implying that $K_\Gamma^{(\hat{x})} \subset \{y \in \mathbb{R}^2 : \inf(\hat{x} \cdot \Gamma) \leq \hat{x} \cdot y \leq \sup(\hat{x} \cdot \Gamma)\}$. Reconstructions from nonobservable angles $\theta \in (0, \pi/2) \cup (3\pi/2, 2\pi)$ are illustrated in Figure 11. The values are still very small and cannot reconstruct the strip $\{y \in \mathbb{R}^2 : \inf(\hat{x} \cdot \Gamma) \leq \hat{x} \cdot y \leq \sup(\hat{x} \cdot \Gamma)\}$.

Example 3: *A piecewise linear curve in* $\mathbb{R}^2$. We first remark that the analysis performed in sections 2–4 carry over to piecewisely C^1-smooth orbit functions. Complexity arises only from the definition of the division points made in Definition 3.1, where the discontinuity points of $h'(t)$ should be taken into account. Assume that the trajectory of the moving source $a(t)$ is given by

$$a(t) = \begin{cases} (-t + 3, -t + 3), & t \in [0, 1], \\ (t + 1, -t + 3), & t \in [1, 2]. \end{cases}$$

Let $\hat{x} = (\cos\theta, \sin\theta)$, $\theta \in [0, 2\pi)$, be the observation direction. We first calculate the observable and nonobservable directions. Note that $T = 2$. Evidently,

$$h(t) = t + \hat{x} \cdot a(t) = \begin{cases} t(1 - \cos\theta - \sin\theta) + 3(\cos\theta + \sin\theta), & t \in [0, 1], \\ t(1 + \cos\theta - \sin\theta) + \cos\theta + 3\sin\theta, & t \in [1, 2], \end{cases}$$

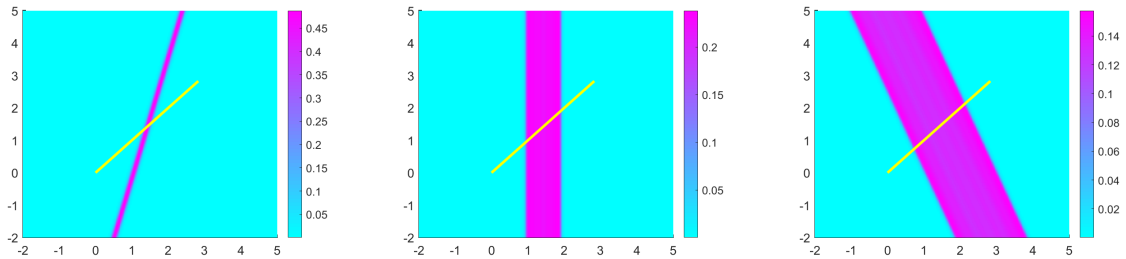

(a) $\theta = 11\pi/12$ (b) $\theta = 8\pi/8$ (c) $\theta = 9\pi/8$

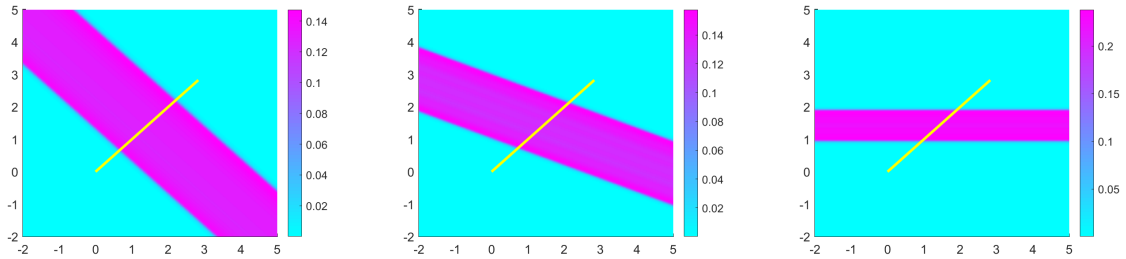

(d) $\theta = 10\pi/8$ (e) $\theta = 11\pi/8$ (f) $\theta = 12\pi/8$

Figure 8. *Reconstruction from a single observable direction* $\hat{x} = (\cos\theta, \sin\theta)$ *with* $\theta \in [11\pi/12, 19\pi/12]$ *for a straight line segment* $a(t) = (2\sqrt{2}t, 2\sqrt{2}t)$ *with* $t \in [1,2]$. *Since* $h'(t) < 0$, *the strip* $K_\Gamma^{(\hat{x})}$ *is a subset of* $\{y \in \mathbb{R}^2 : \hat{x} \cdot y \in \hat{x} \cdot \Gamma\}$.

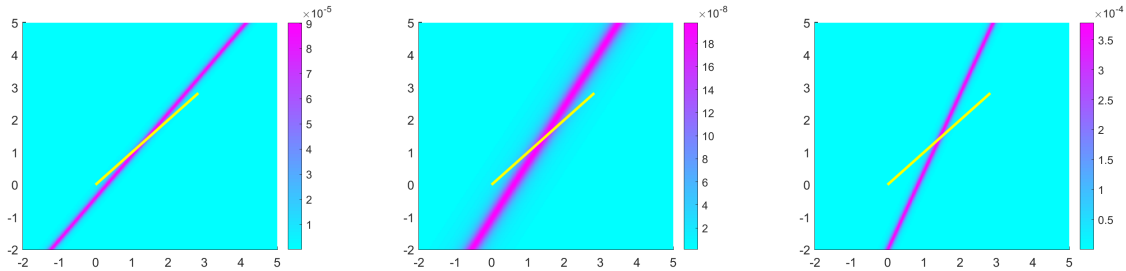

(a) $\theta = 19\pi/24$ (b) $\theta = 20\pi/24$ (c) $\theta = 21\pi/24$

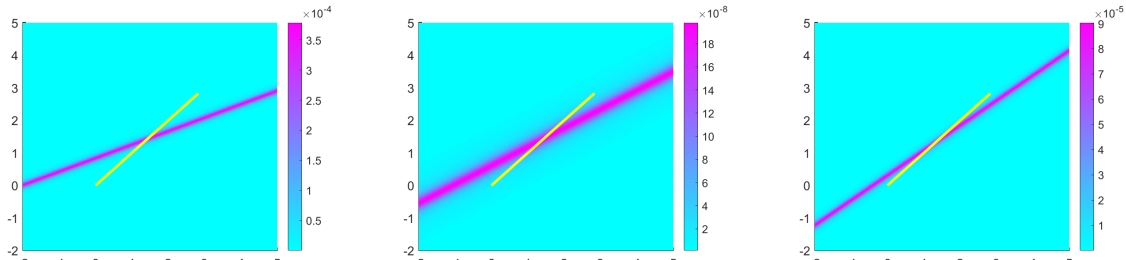

(d) $\theta = 39\pi/24$ (e) $\theta = 40\pi/24$ (f) $\theta = 41\pi/24$

Figure 9. *Reconstruction from a single nonobservable direction* $\hat{x} = (\cos\theta, \sin\theta)$ *with* $\theta \in (3\pi/4, 11\pi/12) \cup (19\pi/12, 7\pi/4)$ *for a straight line segment* $a(t) = (2\sqrt{2}t, 2\sqrt{2}t)$ *with* $t \in [1,2]$.

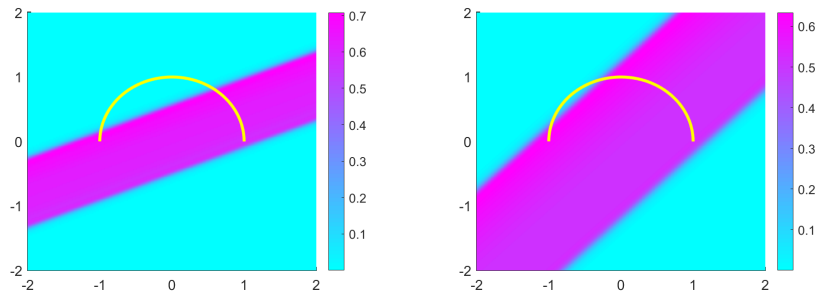

(a) $\theta = 5\pi/8$ (b) $\theta = 6\pi/8$

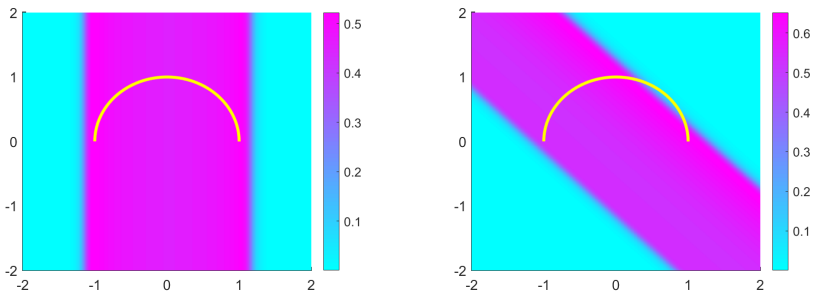

(c) $\theta = 8\pi/8$ (d) $\theta = 10\pi/8$

Figure 10. *Reconstruction from a single observable direction* $\hat{x} = (\cos\theta, \sin\theta)$ *with* $\theta \in [\pi/2, 3\pi/2]$ *for an arc* $a(t) = (\cos t, \sin t)$ *with* $t \in [0, \pi]$.

and thus

$$h'(t) = 1 + \hat{x} \cdot a'(t) = \begin{cases} 1 - \cos\theta - \sin\theta, & t \in (0,1), \\ 1 + \cos\theta - \sin\theta, & t \in (1,2). \end{cases}$$

Since $h'(t) \equiv 0$ in some interval when $\theta = 0, \pi/2$, and π, we need to consider the following six cases separately.

(1) $\theta = 0$**.** We have $h'(t) = 0$ for $t \in (0,1)$ and $h'(t) > 0$ for $t \in (1,2)$. This gives $3 \le h(t) \le 5$ for $t \in (0,2)$, implying $\xi_{\max}^{(\hat{x})} - \xi_{\min}^{(\hat{x})} = T$. Thus, $\hat{x} = (1,0)$ is an observable direction.

(2) $\theta \in (0, \pi/2)$. We have $h'(t) < 0$ for $t \in (0,1)$ and $h'(t) > 0$ for $t \in (1,2)$. Therefore, for $\xi = h(t), t \in (0,2)$, it holds that

$$\begin{aligned} \xi &\in [1 + 2(\cos\theta + \sin\theta), 3(\cos\theta + \sin\theta)] \cup [1 + 2(\cos\theta + \sin\theta), 2 + 3\cos\theta - \sin\theta] \\ &= [1 + 2(\cos\theta + \sin\theta), \max\{3(\cos\theta + \sin\theta), 2 + 3\cos\theta - \sin\theta\}]. \end{aligned}$$

Consequently, $\xi_{\max}^{(\hat{x})} - \xi_{\min}^{(\hat{x})} = \max\{\cos\theta + \sin\theta - 1, 1 + \cos\theta - 3\sin\theta\} < T = 2$. Thus, each $\hat{x}$ with $\theta \in (0, \pi/2)$ is nonobservable.

(3) $\theta = \pi/2$. We have $h'(t) = 0$ for $t \in (0,1)$ and $h'(t) = 0$ for $t \in (1,2)$, implying that $h(t) \equiv 3$. Hence, $\xi_{\max}^{(\hat{x})} - \xi_{\min}^{(\hat{x})} = 0 < T$. Thus, $\hat{x} = (0,1)$ is nonobservable.

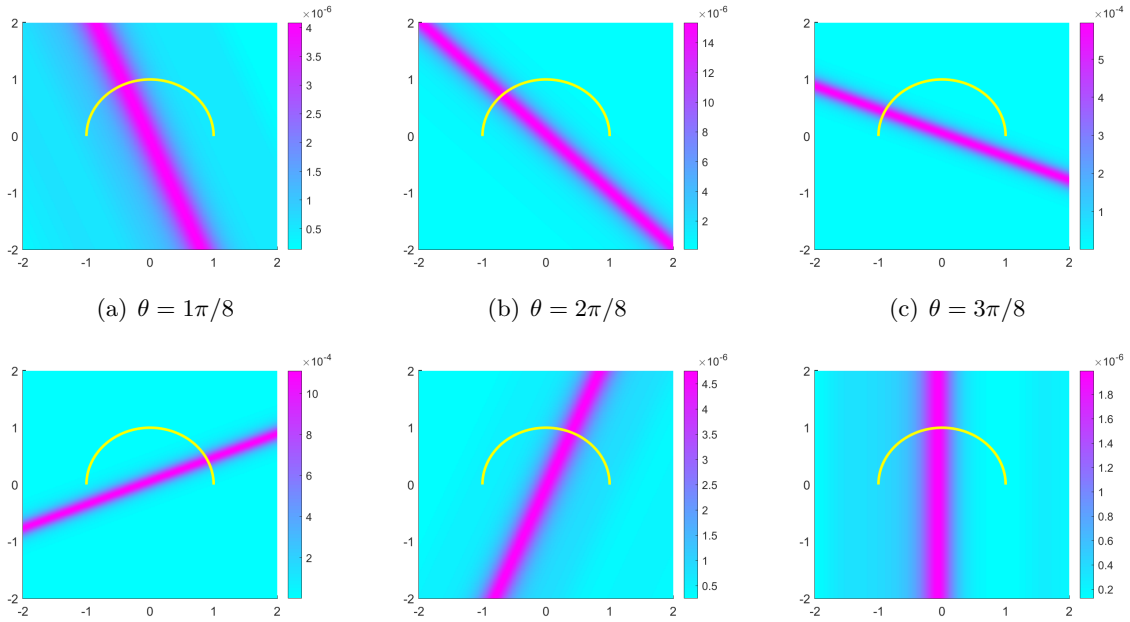

(a) $\theta = 1\pi/8$ (b) $\theta = 2\pi/8$ (c) $\theta = 3\pi/8$

(d) $\theta = 13\pi/8$ (e) $\theta = 15\pi/8$ (f) $\theta = 16\pi/8$

Figure 11. *Reconstruction from a single nonobservable direction* $\hat{x} = (\cos\theta, \sin\theta)$ *with* $\theta \in (0, \pi/2) \cup (3\pi/2, 2\pi)$ *for an arc* $a(t) = (\cos t, \sin t)$ *with* $t \in [0, \pi]$.

(4) $\theta \in (\pi/2, \pi)$. We have $h'(t) > 0$ for $t \in (0,1)$ and $h'(t) < 0$ for $t \in (1,2)$. Hence, if $\xi = h(t)$ for some $t \in (0,2)$, then

$$\begin{aligned}\xi &\in [3(\cos\theta + \sin\theta), 1 + 2(\cos\theta + \sin\theta)] \cup [2 + 3\cos\theta - \sin\theta, 1 + 2(\cos\theta + \sin\theta)] \\ &= [\min\{3(\cos\theta + \sin\theta), 2 + 3\cos\theta - \sin\theta\}, 1 + 2(\cos\theta + \sin\theta)].\end{aligned}$$

In this case, we get $\xi_{\max}^{(\hat{x})} - \xi_{\min}^{(\hat{x})} = \max\{1 - \cos\theta - \sin\theta, 3\sin\theta - \cos\theta - 1\} < T$. Thus, the direction $\hat{x}$ with $\theta \in (\pi/2, \pi)$ is nonobservable.

(5) $\theta = \pi$. We have $h'(t) > 0$ in $(0,1)$ and $h'(t) = 0$ in $(1,2)$, implying $-3 \le h(t) \le -1$ for $t \in (0,2)$. Thus $\xi_{\max}^{(\hat{x})} - \xi_{\min}^{(\hat{x})} = 2$, and $\hat{x} = (-1, 0)$ is an observable direction.

(6) $\theta \in (\pi, 2\pi)$. We have $h'(t) > 0$ for $t \in (0,1)$ and $h'(t) > 0$ for $t \in (1,2)$. For $\xi = h(t)$ we have

$$\begin{aligned}\xi &\in [3(\cos\theta + \sin\theta), 1 + 2(\cos\theta + \sin\theta)] \cup [1 + 2(\cos\theta + \sin\theta), 2 + 3\cos\theta - \sin\theta] \\ &= [3(\cos\theta + \sin\theta), 2 + 3\cos\theta - \sin\theta],\end{aligned}$$

implying that $\xi_{\max}^{(\hat{x})} - \xi_{\min}^{(\hat{x})} = 2 - 4\sin\theta > 2$. Therefore, each direction $\hat{x}$ with $\theta \in (0, \pi)$ is observable.

Summing up, we conclude that $[\pi, 2\pi]$ consists of observable angles and $(0, \pi)$ the nonobservable ones. In Figure 12, we plot the indicator functions for different observable angles in $[\pi, 2\pi]$. In subfigures (b), (c), (d), and (e), the reconstructed strip $K_\Gamma^{(\hat{x})}$ coincides with

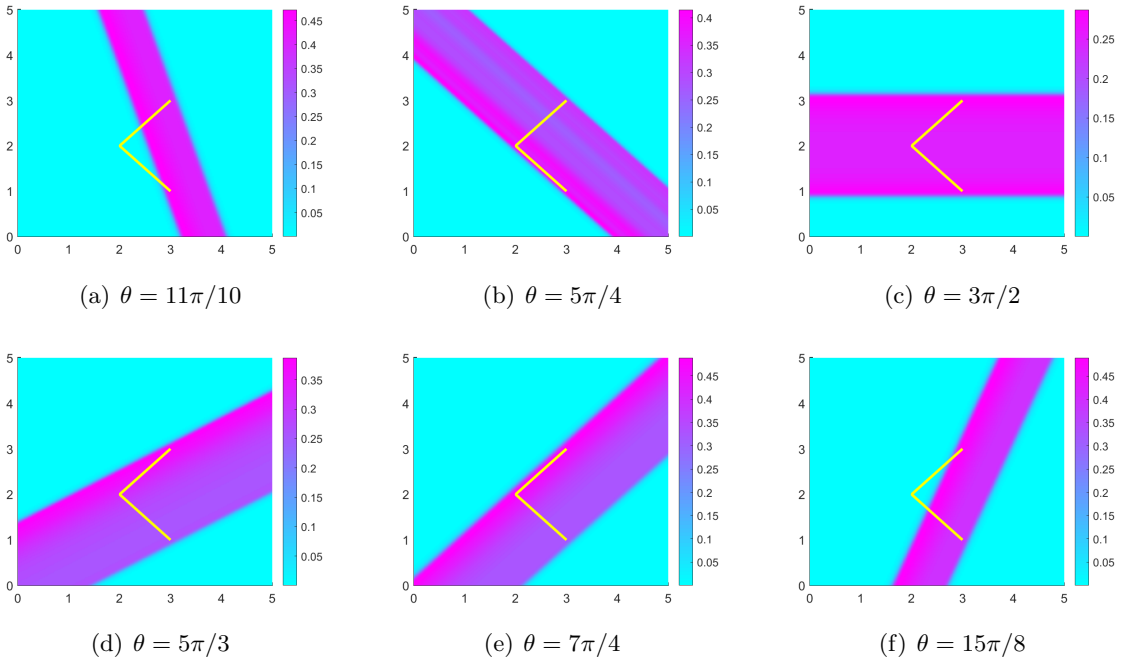

(a) $\theta = 11\pi/10$ (b) $\theta = 5\pi/4$ (c) $\theta = 3\pi/2$

(d) $\theta = 5\pi/3$ (e) $\theta = 7\pi/4$ (f) $\theta = 15\pi/8$

Figure 12. *Reconstruction from a single observable direction* $\hat{x} = (\cos\theta, \sin\theta)$ *with* $\theta \in [\pi, 2\pi]$ *for a broken line segment* $a(t) = (-t+3, -t+3)$ *with* $t \in [0,1]$ *and* $a(t) = (t+1, -t+3)$ *with* $t \in [1,2]$ *in* $\mathbb{R}^2$.

$\{y \in \mathbb{R}^2 : \inf(\hat{x}\cdot\Gamma) \le \hat{x}\cdot y \le \sup(\hat{x}\cdot\Gamma)\}$ for all $t \in [0,2]$ and $\theta = 5\pi/4$, $3\pi/2$, $5\pi/3$, and $7\pi/4$. The strips $K_\Gamma^{(\hat{x})}$ in subfigures (a) and (f) are subsets of $\{y \in \mathbb{R}^2 : \sup(\hat{x}\cdot\Gamma) \le \hat{x}\cdot y \le \inf(\hat{x}\cdot\Gamma)\}$ for all $t \in [0,2]$ and $\theta = 11\pi/10$ and $15\pi/8$. In Figure 13 we show reconstructions from nonobservable angles $\theta \in (0,\pi)$.

Example 4: *A straight line segment in* $\mathbb{R}^3$. Consider a straight line segment in $\mathbb{R}^3$ parameterized by $a(t) = (0,0,t)$, $t \in [0,1]$, and write the observation direction as $\hat{x} = (\sin\theta\cos\varphi, \sin\theta\sin\varphi, \cos\theta)$, $\theta \in [0,\pi]$, $\varphi \in [0,2\pi)$. Then,

$$h(t) = t + \hat{x}\cdot a(t) = t(1+\cos\theta), \qquad h'(t) = 1 + \hat{x}\cdot a'(t) = 1+\cos\theta.$$

It follows that $h'(t) > 0$ for all $t \in [t_{\min}, t_{\max}]$. Hence $\hat{x}$ is a nonobservable direction only if $\cos\theta < 0$, that is, $\theta \in (\pi/2, \pi)$, and $\hat{x}$ is an observable direction if $\theta \in [0, \pi/2]$. In Figure 14, we illustrate two planes perpendicular to the observable direction, between which the trajectory of the moving source is located. Figure 15 presents slices of the smallest hyperspace at $x_1 = 0$ and $x_3 = -2$ reconstructed from the data of different observable directions. We conclude that the trajectory of the moving source lies perfectly between the two planes that are perpendicular to the observation direction. It demonstrates effectiveness of our algorithm for imaging a straight line segment in $\mathbb{R}^3$. Since the smallest hyperspace perpendicular to the observable direction and containing the trajectory of the moving point source can be recovered in $\mathbb{R}^3$, there exists a strip on every slice projected by the hyperspace. If we connect the edges of the two strips in Figures 15(h) and (i), we get hyperplanes similar to those in Figure 14. In

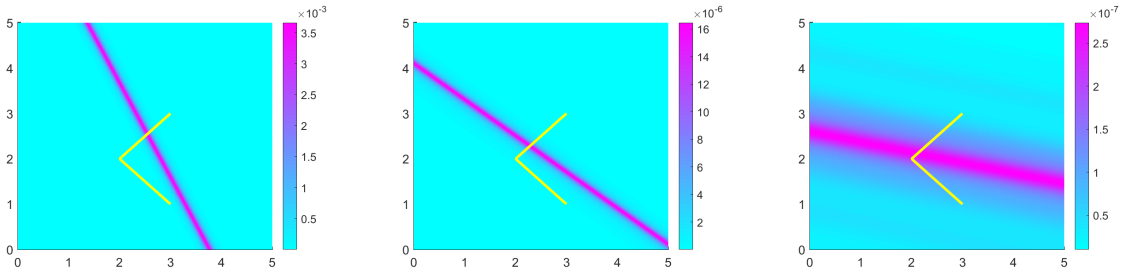

(a) $\theta = \pi/7$ (b) $\theta = 2\pi/7$ (c) $\theta = 3\pi/7$

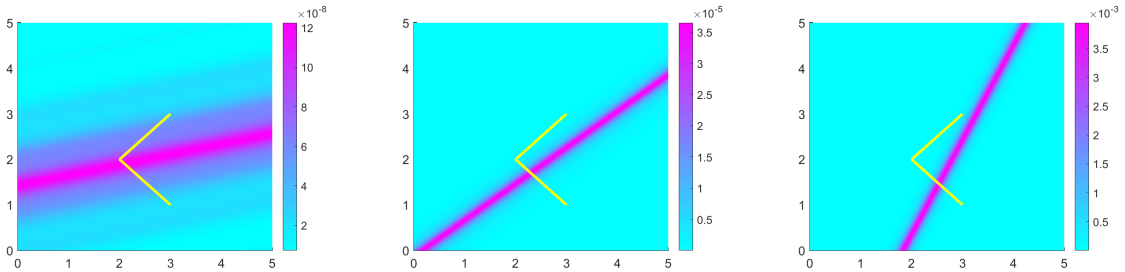

(d) $\theta = 4\pi/7$ (e) $\theta = 5\pi/7$ (f) $\theta = 6\pi/7$

Figure 13. *Reconstruction from a single nonobservable direction* $\hat{x} = (\cos\theta, \sin\theta)$ *with* $\theta \in (0, \pi)$ *for a piecewise linear curve* $a(t) = (-t+3, -t+3)$ *with* $t \in [0,1]$ *and* $a(t) = (t+1, -t+3)$ *with* $t \in [1,2]$ *in* $\mathbb{R}^2$.

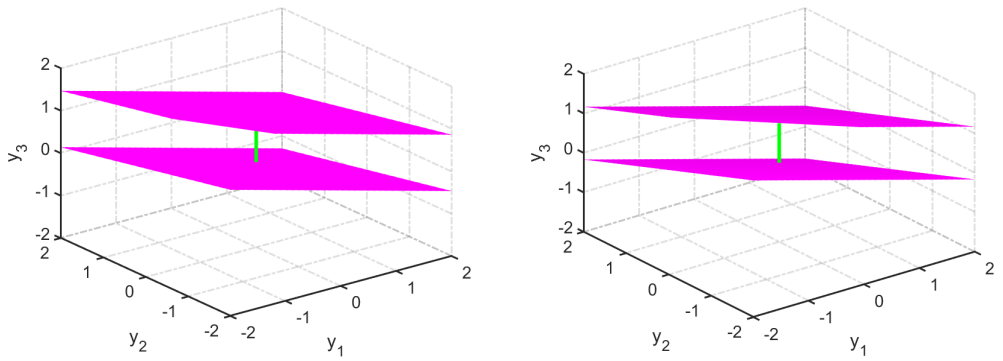

(a) $\phi = \pi/6, \theta = \pi/8$ (b) $\phi = \pi/4, \theta = \pi/6$

Figure 14. *Illustration of the hyperplanes perpendicular to the observable direction* $\hat{x} = (\sin\theta\cos\phi, \sin\theta\sin\phi, \cos\phi)$. *Here we take isosurface level* $= 0.02$.

Figure 16, we plot the indicator functions with different nonobservable directions. The values of the indicator function are much smaller than 10^{-3}.

Remark 5.1. Let us discuss the width $l^{(\hat{x})}$ of the strip $K_\Gamma^{(\hat{x})}$. If $\hat{x}$ is observable and $h'(t) \geq 1$, we have $l^{(\hat{x})} = \sup(\hat{x}\cdot\Gamma) - \inf(\hat{x}\cdot\Gamma)$; if $\hat{x}$ is observable and $h'(t) \geq 1$ doesn't hold for all $(t_{\min}, t_{\max})$, then $l^{(\hat{x})} < \sup(\hat{x}\cdot\Gamma) - \inf(\hat{x}\cdot\Gamma)$; if the direction $\hat{x}$ in the latter case is getting

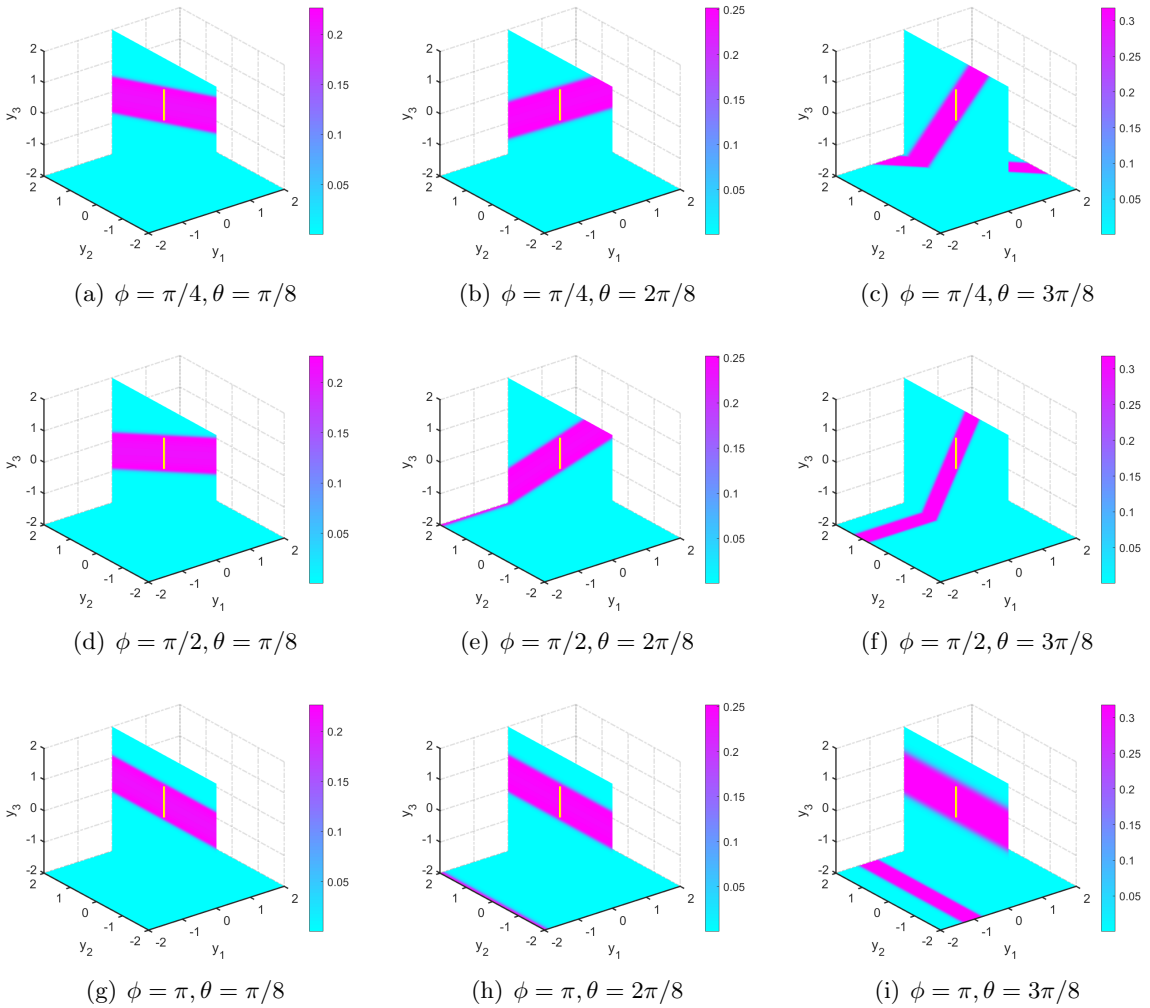

(a) $\phi = \pi/4, \theta = \pi/8$ (b) $\phi = \pi/4, \theta = 2\pi/8$ (c) $\phi = \pi/4, \theta = 3\pi/8$

(d) $\phi = \pi/2, \theta = \pi/8$ (e) $\phi = \pi/2, \theta = 2\pi/8$ (f) $\phi = \pi/2, \theta = 3\pi/8$

(g) $\phi = \pi, \theta = \pi/8$ (h) $\phi = \pi, \theta = 2\pi/8$ (i) $\phi = \pi, \theta = 3\pi/8$

Figure 15. *Reconstruction from a single observable direction* $\hat{x} = (\sin\theta\cos\varphi, \sin\theta\sin\varphi, \cos\theta)$ *with* $\theta \in [0, \pi/2]$ *and* $\phi \in [0, 2\pi)$ *for a straight line segment* $a(t) = (0, 0, t)$ *with* $t \in [0, 1]$ *in* $\mathbb{R}^3$. *Here we take slices at* $x_1 = 0$ *and* $x_3 = -2$.

closer to some nonobservable direction, our numerical tests show that $l^{(\hat{x})}$ tends to be thinner and thinner.

Example 5: *Two straight line segments in* $\mathbb{R}^2$. Suppose that two acoustic point sources are moving along the straight lines $a(t) = (-1, 0.5t - 2) \in \mathbb{R}^2$ and $b(t) = (1, 0.5t + 1.5) \in \mathbb{R}^2$ for $t \in [1, 3]$, respectively. Choose the search domain as the square $[-4, 4] \times [-4, 4]$. By Definition 3.6 and the proof of Lemma 3.8, we obtain the observable directions $\hat{x} = (\cos\theta, \sin\theta)$ with $\theta \in [0, \pi]$ and the nonobservable directions $\hat{x} = (\cos\theta, \sin\theta)$ with $\theta \in (\pi, 2\pi)$ for both trajectories. Here we define two functions $h_a^{(\hat{x})}(t) := t + \hat{x} \cdot a(t)$ and $h_b^{(\hat{x})}(t) := t + \hat{x} \cdot b(t)$ and two intervals

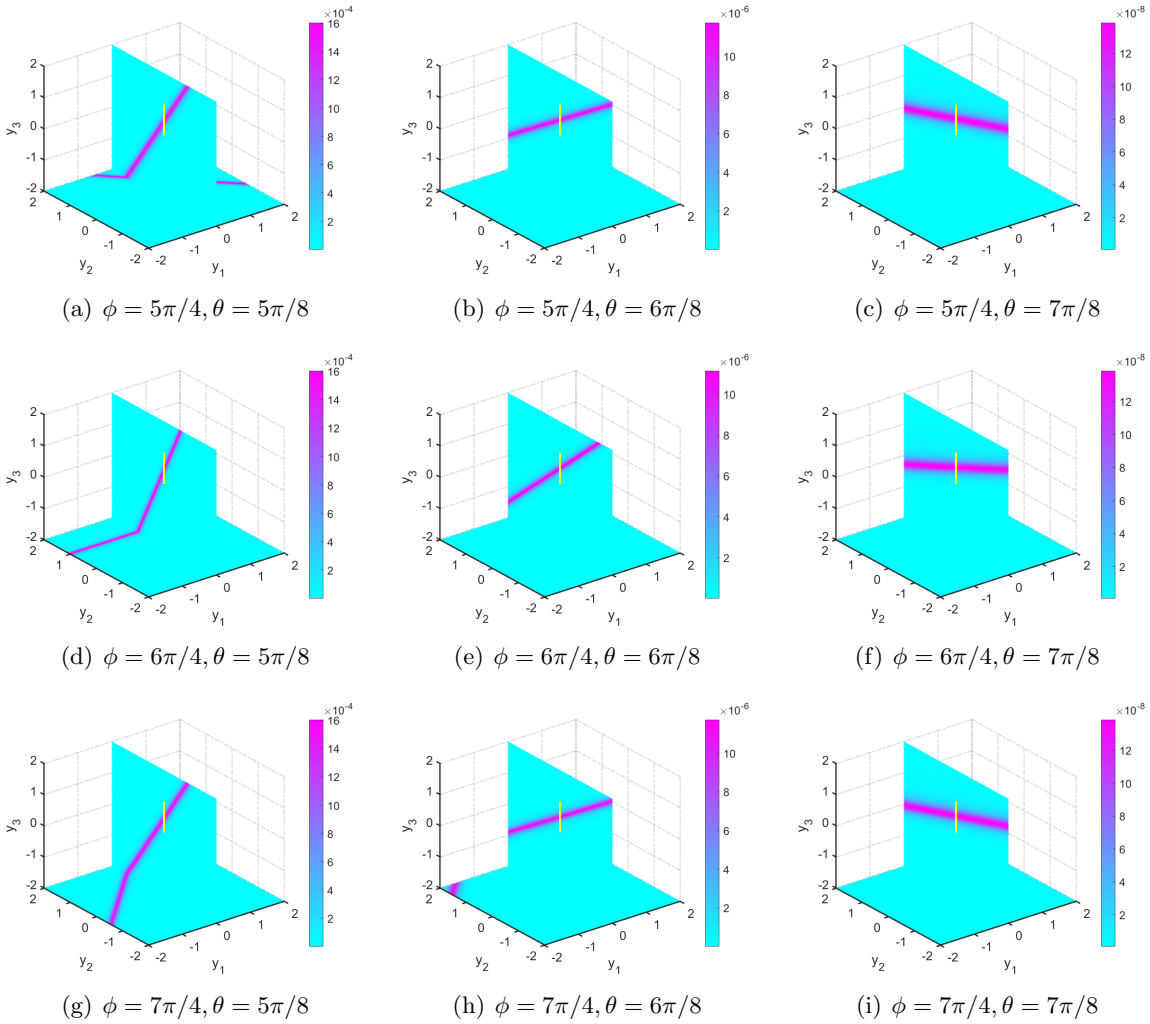

(a) $\phi = 5\pi/4, \theta = 5\pi/8$ (b) $\phi = 5\pi/4, \theta = 6\pi/8$ (c) $\phi = 5\pi/4, \theta = 7\pi/8$

(d) $\phi = 6\pi/4, \theta = 5\pi/8$ (e) $\phi = 6\pi/4, \theta = 6\pi/8$ (f) $\phi = 6\pi/4, \theta = 7\pi/8$

(g) $\phi = 7\pi/4, \theta = 5\pi/8$ (h) $\phi = 7\pi/4, \theta = 6\pi/8$ (i) $\phi = 7\pi/4, \theta = 7\pi/8$

Figure 16. *Reconstruction from a single nonobservable direction* $\hat{x} = (\cos\theta, \sin\theta)$ *with* $\theta \in (\pi/2, \pi)$ *and* $\phi \in [0, 2\pi)$ *for a straight line segment* $a(t) = (0, 0, t)$ *with* $t \in [0, 1]$ *in* $\mathbb{R}^3$. *Here we take slices at* $x = 0$ *and* $z = -2$.

$$I_a^{(\hat{x})} := \left[\inf_{t\in[1,3]} h_a(t), \sup_{t\in[1,3]} h_a(t) \right], \; I_b^{(\hat{x})} := \left[\inf_{t\in[1,3]} h_b(t), \sup_{t\in[1,3]} h_b(t) \right].$$

By Lemma 3.3, we know that if $I_a^{(\hat{x})} \bigcap I_b^{(\hat{x})} = \emptyset$, the two trajectories can be well separated. The angles of observable directions are taken as $\theta = 0, \pi/8, 2\pi/8, 3\pi/8, 6\pi/8, 7\pi/8$. In Table 1, we compute the intervals $I_a^{(\hat{x})}$ and $I_b^{(\hat{x})}$ for these observable angles. It is clear that the two trajectories can be well separated for $\theta = \pi/8, 2\pi/8, 3\pi/8$ and there exists some overlap for $\theta = 0, 6\pi/8, 7\pi/8$ in Table 1. The numerical results presented in Figures 17(b), (c), and (d) show that the two different trajectories can be well separated even though there is a

Table 1
The intervals $I_a^{(\hat{x})}$ and $I_b^{(\hat{x})}$ for different observable angles θ.

θ	$\left[\inf_{t\in[1,3]} h_a^{(\hat{x})}(t),\ \sup_{t\in[1,3]} h_a^{(\hat{x})}(t)\right]$	$\left[\inf_{t\in[1,3]} h_b^{(\hat{x})}(t),\ \sup_{t\in[1,3]} h_b^{(\hat{x})}(t)\right]$
0	[0.0000, 2.0000]	[2.0000, 4.0000]
$1\pi/8$	[-0.4979, 1.8848]	[2.6892, 5.0719]
$2\pi/8$	[-0.7678, 1.9393]	[2.6892, 5.0719]
$3\pi/8$	[-0.7685, 2.1554]	[3.2304, 6.1543]
$6\pi/8$	[0.6464, 3.3536]	[1.7071, 4.4142]
$7\pi/8$	[1.3499, 3.7325]	[0.8415, 3.2242]

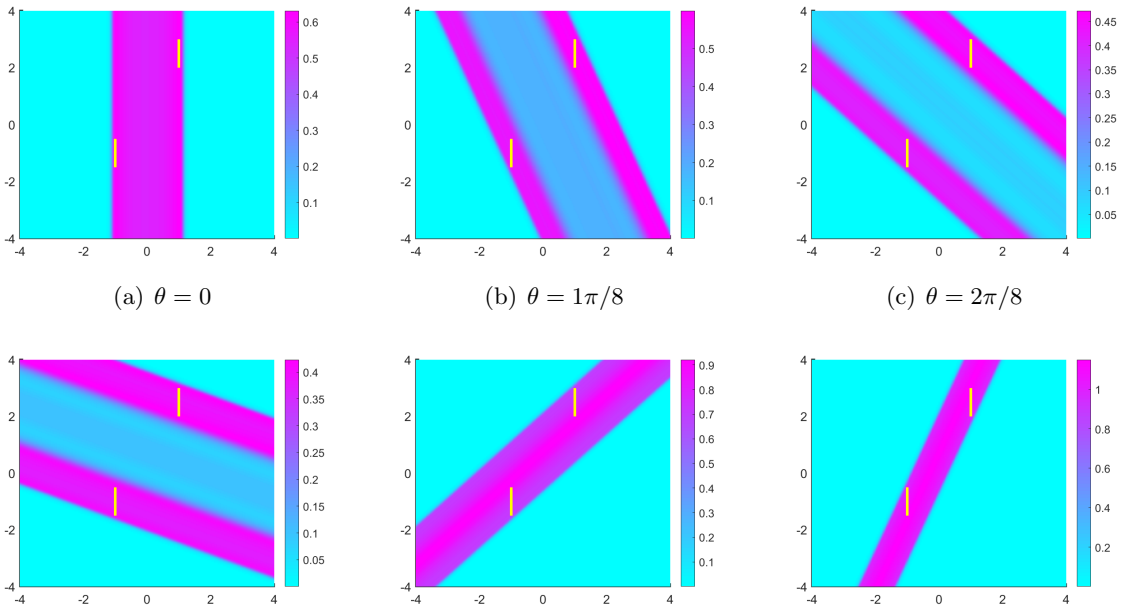

(a) $\theta = 0$ (b) $\theta = 1\pi/8$ (c) $\theta = 2\pi/8$

(d) $\theta = 3\pi/8$ (e) $\theta = 6\pi/8$ (f) $\theta = 7\pi/8$

Figure 17. *Reconstruction from a single observable direction $\hat{x} = (\cos\theta, \sin\theta)$ with $\theta \in [0, \pi]$ for two straight line segments $a(t) = (-1, 0.5t - 2)$ and $b(t) = (1, 0.5t + 1.5)$ with $t \in [1, 3]$ in $\mathbb{R}^2$.*

little disturbance between the two trajectories. The numerical results in Figures 17(a), (e), and (f) illustrate that $\theta = 0, 6\pi/8, 7\pi/8$ are observable angles, but there are overlaps of the smallest strips for different trajectories and we cannot identify the two trajectories with a single observable direction. All the numerical results verify the theoretical results.

5.2. Multiple observation directions. In this subsection, we continue the two-dimensional Examples 1, 2, and 3 but with multifrequency far-field data measured at sparse directions. We should truncate the indicator function (4.2) by

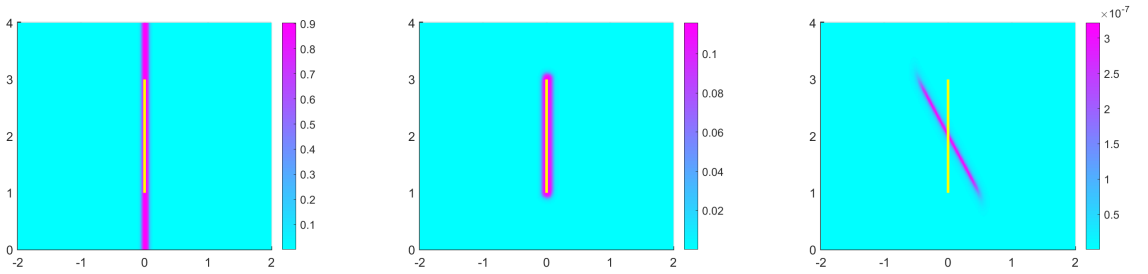

(a) $M' = 1.5$ (b) $M' = 3.5 \times 10^3$ (c) $M' = 10^7$

Figure 18. *Reconstruction from multiple observation directions* $\hat{x} = (\cos\theta, \sin\theta)$ *with* $\theta \in [0, 2\pi)$ *for a straight line segment* $a(t) = (0, t)$ *with* $t \in [1, 3]$. *We set the observation directions as* $\theta = (j-1) * 2\pi/7$, $j = 1, \ldots, 7$, *with different thresholds.* (a) $M' = 1.5$; (b) $M' = 3.5 \times 10^3$; (c) $M' = 10^7$.

$$W(y) := \left[\sum_{j=1}^{M} \sum_{n=1}^{N} \frac{\left| \phi_y^{(\hat{x}_j)} \cdot \overline{\psi_n^{(\hat{x}_j)}} \right|^2}{|\lambda_n^{(\hat{x}_j)}|} \right]^{-1}, \quad y \in \mathbb{R}^2, \tag{5.7}$$

where $M > 0$ denotes the number of sparse observation directions equally lying on $\mathbb{S}^1$, the test function $\phi_y^{(\hat{x}_j)}$ is again given by (5.5), and $\{(\lambda_n^{(\hat{x}_j)}, \psi_n^{(\hat{x}_j)}) : n = 1, \ldots, N\}$ denote an eigensystem of the operator $(\mathcal{F}^{(\hat{x}_j)})_{\#}$. It is worth noting that $\hat{x}_j$ $(j = 1, 2, \ldots, M)$ may contain both observable and nonobservable directions. We set a threshold $M' > 0$ to remove the contributions of the terms like

$$\tilde{w}_j = \sum_{n=1}^{N} \frac{\left| \phi_y^{(\hat{x}_j)} \cdot \overline{\psi_n^{(\hat{x}_j)}} \right|^2}{|\lambda_n^{(\hat{x}_j)}|}, \quad j = 1, 2, \ldots, W,$$

to the sum in (5.7). More precisely, if $\min(\tilde{w}_j(y)) > M'$, the direction $\hat{x}_j$ can be considered as a nonobservable direction by the second assertion of Theorem 4.1. Here, the threshold M' is crucial. In Figure 18, we reconstruct the straight line segment of Example 1 from multiple observation directions $\hat{x} = (\cos\theta, \sin\theta)$ with $\theta = (j-1) * 2\pi/7$, $j = 1, \ldots, 7$, but with different thresholds. The observable direction angles are $\theta = 0, 2\pi/7, 4\pi/7, 6\pi/7$. If the threshold is selected to be small, an observable direction will be mistaken as the nonobservable direction, resulting in the loss of some measurement data. Only one strip perpendicular to the observation direction with $\theta = 0$ is observed in Figure 18(a). On the other hand, if the threshold is chosen to be sufficiently large, the contribution of nonobservable directions will be retained, affecting the accuracy of reconstruction and even yielding no information on the trajectory. From Figure 18(c), one cannot get any information on the trajectory. Therefore, in our numerical examples, the choice of the magnitude of the threshold relies on the indicator function at a single nonobservable direction. Figure 18(c) shows a good reconstruction of the trajectory. In the following numerical examples, the threshold value is set as $M' = 3.5 \times 10^3$.

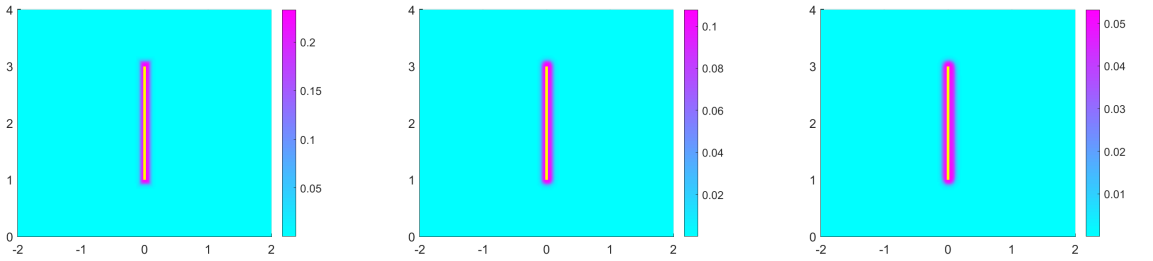

(a) $M = 2$ (b) $M = 4$ (c) $M = 8$

Figure 19. *Reconstruction from multiple observation directions* $\hat{x} = (\cos\theta, \sin\theta)$ *with* $\theta \in [0, 2\pi)$ *for a straight line segment* $a(t) = (0, t)$ *with* $t \in [1, 3]$. *Here* M *denotes the number of directions.* (a) $\theta = 0, \pi/2$; (b) *and* (c) $\theta = (j-1) * 2\pi/M$, $j = 1, \ldots, M$.

We present in Figure 19 a visualization of the reconstructed trajectory for orbit functions $a(t) = (0, t)$ with $t \in [1, 3]$ with multiple observation directions. For $M = 2, 4, 8$, there exist one direction perpendicular to the trajectory and one parallel to the trajectory, and the intersections of the strips $K_\Gamma^{(\hat{x}_j)}$ always reflect the trajectory of the moving source. Since $h'(t) > 0$ for all observable directions in Example 1, the trajectory can be perfectly reconstructed from the data taken on sparse observation directions.

However, in the case of the line segment in Example 3 or the arc in Example 4, we can only get partial information on the trajectory. From Figures 20 and 21, one can only get the starting and ending points of the trajectory, although the data of multiple directions are put into use. This is due to the existence of $\hat{x}_j$ satisfying $K_\Gamma^{(\hat{x}_j)} \subset \{y \in \mathbb{R}^2 : \inf(\hat{x} \cdot \Gamma) \le \hat{x} \cdot y \le \sup(\hat{x} \cdot \Gamma)\}$. For such observation directions, the width of the reconstructed strip $K_\Gamma^{(\hat{x}_j)}$ is very small. Hence, the intersection of $K_\Gamma^{(\hat{x}_j)}$ always appears like a line segment connecting the starting and the ending points of the trajectory.

5.3. Reconstructions from noisy data. We test the sensitivity of the algorithm with respect to the noisy data. Consider Case 1 in Example 1 in section 5.1 for recovering a line segment. The far-field data are polluted by Gaussian noise in the form of

$$w_\delta^\infty(\hat{x}, k) := \mathrm{Re}\,[w^\infty(\hat{x}, k)]\,(1 + \delta\,\gamma_1) + \mathrm{Im}[w^\infty(\hat{x}, k)]\,(1 + \delta\,\gamma_2),$$

where $\delta > 0$ denotes the noise level and $\gamma_j \in [-1, 1]$ $(j = 1, 2)$ are Gaussian random variables.

We set $\delta = 1\%$ and plot the indicator functions in Figure 22 using one and sparse observation directions. It turns out that the proposed scheme is rather sensitive to noise. Even at the noise level 1%, one can only get a rough location of the trajectory of the moving source using the data measured at sparse directions. This shows that our inverse problems are severely ill-posed. However, a quantitative characterization of the ill-posed nature remains unclear to us.

To explain why our method is sensitive to noise, we take the numerical test in Figure 22(a) as an example and list the eigenvalues of the unpolluted and polluted far-field operators in

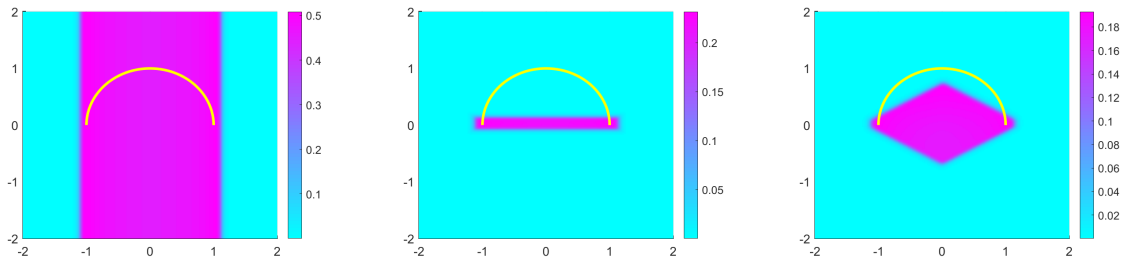

(a) $M = 2$ (b) $M = 4$ (c) $M = 6$

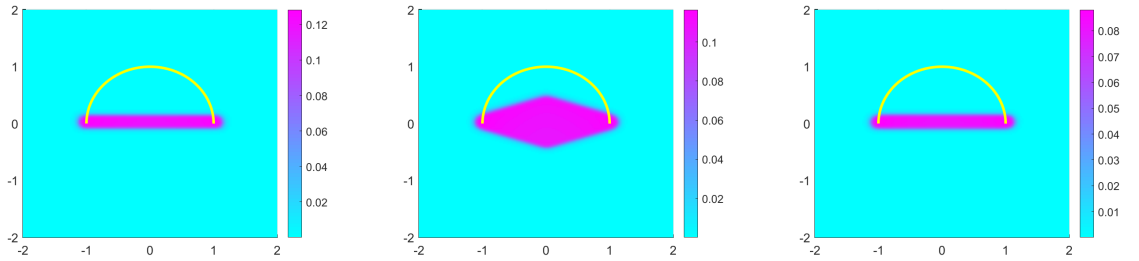

(d) $M = 8$ (e) $M = 10$ (f) $M = 12$

Figure 20. *Reconstruction from multiple observation directions* $\hat{x} = (\cos\theta, \sin\theta)$ *with* $\theta \in (0, 2\pi)$ *for an arc* $a(t) = (\cos t, \sin t)$ *with* $t \in [0, \pi]$. *Here* M *is the number of directions.* $\theta = (j-1) * 2\pi/M$, $j = 1, 2, \ldots, M$.

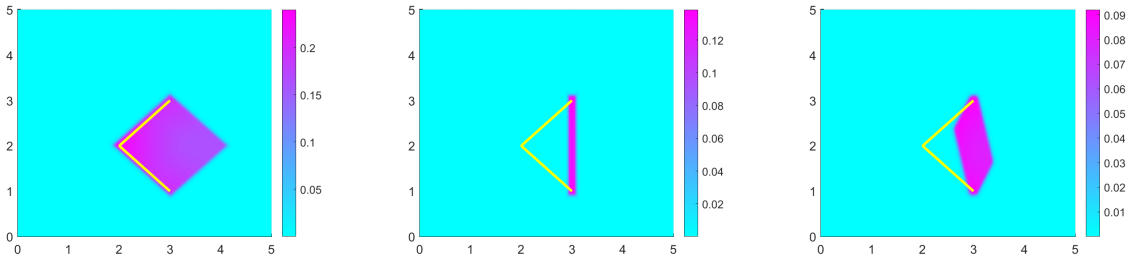

(a) $M = 2$ (b) $M = 4$ (c) $M = 7$

Figure 21. *Reconstruction from multiple observation directions* $\hat{x} = (\cos\theta, \sin\theta)$ *with* $\theta \in [0, 2\pi)$ *for the piecewise linear curve* $a(t) = (-t + 3, -t + 3)$ *with* $t \in [0, 1]$ *and* $a(t) = (t + 1, -t + 3)$ *with* $t \in [1, 2]$ *in* $\mathbb{R}^2$. *Here* M *is the number of observation directions.* (a) $\theta = 5\pi/4, 7\pi/4$; (b) $\theta = (j-1) * 2\pi/M, j = 1, \ldots, M$; (c) $\theta = 2j * 2\pi/15, j = 1, \ldots, M$.

Table 2. In the noisy case, the far-field operator matrix $F^{(\hat{x})}$ (5.4) and the eigensystem are both polluted. Table 2 shows us that the eigenvalues of the unpolluted far-field operator decay very quickly, but those polluted with 1% noise decay much more slowly. Hence, the noise greatly reduces the decay of the eigenvalues of the far-field matrix, resulting in insignificant differences of indicator functions near boundaries of the strip.

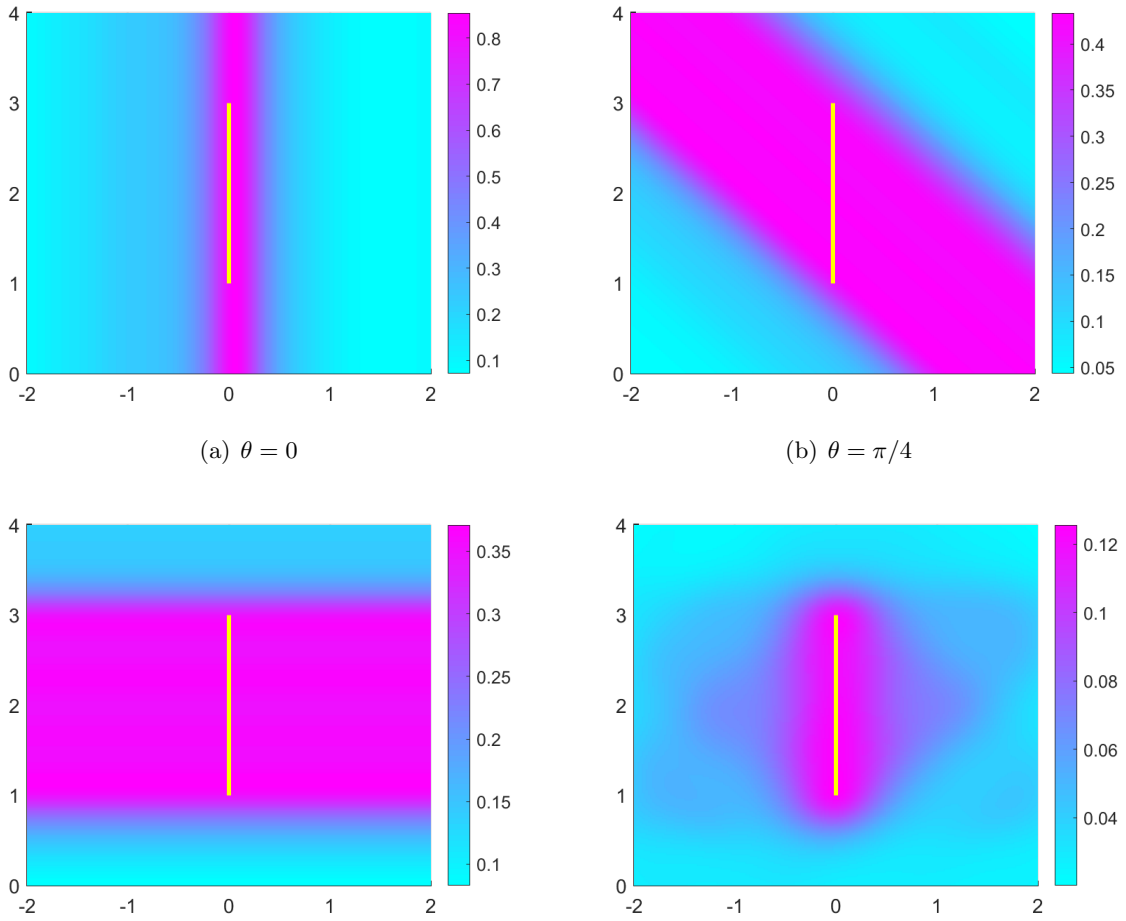

(a) $\theta = 0$ (b) $\theta = \pi/4$

(c) $\theta = \pi/2$ (d) $M = 4$

Figure 22. *Reconstruction of a straight line segment $a(t) = (0, t)$, $t \in [1, 3]$ from noisy data measured at a single observable direction $\hat{x} = (\cos\theta, \sin\theta)$ in* (a), (b), *and* (c). *In* (d), *the polluted far-field data from $M = 4$ directions are used. The noise level is set as $\delta = 1\%$.*

Table 2

The eigenvalues of the far-field operator matrix and that with 1% noise.

λ	λ_1	λ_2	λ_3	λ_4	λ_5	λ_6
original	$4.13 - 2.38i$	$4.93 - 3.43i$	$5.44 - 2.56i$	$1.43 - 0.83i$	$0.18 - 0.11i$	$0.01 - 0.01i$
noisy	$4.25 - 2.38i$	$5.46 - 2.53i$	$4.92 - 3.37i$	$1.41 - 0.85i$	$0.22 - 0.12i$	$0.13 + 0.11i$
λ	λ_7	λ_8	λ_9	λ_{10}	λ_{11}	λ_{12}
original	0	0	0	0	0	0
noisy	$0.08 - 0.17i$	$0.08 - 0.12i$	$-0.19 - 0.07i$	$-0.19 - 0.01i$	$-0.00 + 0.15i$	$-0.08 + 0.09i$
λ	λ_{13}	λ_{14}	λ_{15}	λ_{16}	λ_{17}	λ_{18}
original	0	0	0	0	0	0
noisy	$-0.12 - 0.01i$	$-0.08 - 0.12i$	$-0.02 - 0.10i$	$0.03 + 0.10i$	$-0.01 + 0.02i$	$0.03 + 0.01i$

REFERENCES

[1] A. Alzaalig, G. Hu, X. Liu, and J. Sun, *Fast acoustic source imaging using multifrequency sparse data*, Inverse Problems, 36 (2020), 025009.

[2] B. Chen, Y. Guo, F. Ma, and Y. Sun, *Numerical schemes to reconstruct three-dimensional time-dependent point sources of acoustic waves*, Inverse Problems, 36 (2020), 075009.

[3] M. Cheney and B. Borden, *Imaging moving targets from scattered waves*, Inverse Problems, 24 (2008), 035005.

[4] J. Cooper, *Scattering of plane waves by a moving obstacle*, Arch. Ration. Mech. Anal., 71 (1979), pp. 113–149.

[5] J. Cooper and W. Strauss, *Scattering of waves by periodically moving bodies*, J. Funct. Anal., 47 (1982), pp. 180–229.

[6] A. C. Fannjiang, T. Strohmer, and P. Yan, *Compressed remote sensing of sparse objects*, SIAM J. Imaging Sci., 3 (2010), pp. 595–618, https://doi.org/10.1137/090757034.

[7] J. Fournier, J. Garnier, G. Papanicolaou, and C. Tsogka, *Matched-filter and correlation-based imaging for fast moving objects using a sparse network of receivers*, SIAM J. Imaging Sci., 10 (2017), pp. 2165–2216, https://doi.org/10.1137/17M112364X.

[8] J. Garnier and M. Fink, *Super-resolution in time-reversal focusing on a moving source*, Wave Motion, 53 (2015), pp. 80–93.

[9] R. Griesmaier, *Reconstruction of thin tubular inclusions in three-dimensional domains using electrical impedance tomography*, SIAM J. Imaging Sci., 3 (2010), pp. 340–362, https://doi.org/10.1137/090764074.

[10] R. Griesmaier and M. Hanke, *Multifrequency impedance imaging with multiple signal classification*, SIAM J. Imaging Sci., 8 (2015), pp. 939–967, https://doi.org/10.1137/140992436.

[11] R. Griesmaier and C. Schmiedecke, *A factorization method for multifrequency inverse source problems with sparse far field measurements*, SIAM J. Imaging Sci., 10 (2017), pp. 2119–2139, https://doi.org/10.1137/17M111290X.

[12] H. Guo and G. Hu, *Inverse Wave-Number-Dependent Source Problems for the Helmholtz Equation*, arXiv:2305.07459, 2023.

[13] H. Guo, G. Hu, and M. Zhao, *Direct Sampling Method to Inverse Wave-Number-Dependent Source Problems (Part* I*): Determination of the Support of a Stationary Source*, preprint, arXiv:2212.04806, 2022.

[14] G. Hu, Y. Kian, P. Li, and Y. Zhao, *Inverse moving source problems in electrodynamics*, Inverse Problems, 35 (2019), 075001.

[15] G. Hu, Y. Kian, and Y. Zhao, *Uniqueness to some inverse source problems for the wave equation in unbounded domains*, Acta Math. Appl. Sin. Engl. Ser., 36 (2020), pp. 134–150.

[16] G. Hu, Y. Liu, and M. Yamamoto, *Inverse moving source problem for fractional diffusion(-wave) equations: Determination of orbits*, in Inverse Problems and Related Topics, J. Cheng, S. Lu, and M. Yamamoto, eds., Springer, Singapore, 2020, pp. 81–100.

[17] V. Isakov, *Inverse Source Problems*, AMS, Providence, RI, 1989.

[18] H. A. Jebawy, A. Elbadia, and F. Triki, *Inverse moving point source problem for the wave equation*, Inverse Problems, 38 (2022), 125003.

[19] A. Kirsch and N. Grinberg, *The Factorization Method for Inverse Problems*, Oxford University Press, Oxford, UK, 2008.

[20] A. Lechleiter and D.-L. Nguyen, *Factorization method for electromagnetic inverse scattering from biperiodic structures*, SIAM J. Imaging Sci., 6 (2013), pp. 1111–1139, https://doi.org/10.1137/120903968.

[21] Y. Liu, G. Hu, and M. Yamamoto, *Inverse moving source problem for time-fractional evolution equations: Determination of profiles*, Inverse Problems, 37 (2021), 084001.

[22] Y. Liu, *Numerical schemes for reconstructing profiles of moving sources in (time-fractional) evolution equations*, RIMS Kokyuroku, 2174 (2021), pp. 73–87.

[23] Y. Liu, Y. Guo, and J. Sun, *A deterministic-statistical approach to reconstruct moving sources using sparse partial data*, Inverse Problems, 37 (2021), 065005.

[24] E. Nakaguchi, H. Inui, and K. Ohnaka, *An algebraic reconstruction of a moving point source for a scalar wave equation*, Inverse Problems, 28 (2012), 065018.

[25] T. Ohe, H. Inui, and K. Ohnaka, *Real-time reconstruction of time-varying point sources in a three-dimensional scalar wave equation*, Inverse Problems, 27 (2011), 115011.
[26] F. Qu, J. Yang, and H. Zhang, *Shape reconstruction in inverse scattering by an inhomogeneous cavity with internal measurements*, SIAM J. Imaging Sci., 12 (2019), pp. 788–808, https://doi.org/10.1137/18M1232401.
[27] P. D. Stefanov, *Inverse scattering problem for moving obstacles*, Math. Z., 207 (1991), pp. 461–480.
[28] J. Sylvester and J. Kelly, *A scattering support for broadband sparse far-field measurements*, Inverse Problems, 21 (2005), pp. 759–771.
[29] O. Takashi, *Real-time reconstruction of moving point/dipole wave sources from boundary measurements*, Inverse Probl. Sci. Eng., 28 (2020), pp. 1057–1102.
[30] S. Wang, M. Karamehmedovic, and F. Triki, *Localization of Moving Sources: Uniqueness, Stability and Bayesian Inference*, preprint, arXiv:2204.04465, 2022.